Charles University
Faculty of Science

Study program: Biology
Branch of study: Immunology

Bc. Nikola Ternerová

Fibroblast activation protein and the local immunosuppression in glioblastoma
Fibroblastový aktivační protein a lokální imunosuprese v glioblastomu

Diploma thesis

Supervisor: M.Sc. Lucie Stollinová Šromová, Ph.D.

Prague, 2020

Prohlášení:

Prohlašuji, že jsem závěrečnou práci zpracovala samostatně a že jsem uvedla všechny použité informační zdroje a literaturu. Tato práce ani její podstatná část nebyla předložena k získání jiného nebo stejného akademického titulu.

V Praze, 10.8.2020

Podpis

Acknowledgment

I acknowledge prof. MD Aleksi Šedo, Dr.Sc. for the opportunity of cooperation. I would like to thank my supervisor M.Sc. Lucie Stollinová Šromová, Ph.D. for all the help with the writing of this thesis and doc. MD Petr Bušek, Ph.D., and M.Sc. Magdalena Houdová Megová, Ph.D. for fruitful discussion and helpful advice. I would like to thank my colleague MD Michal Zubaľ for providing data for the characterization of the immunocompetent syngeneic mouse model of glioblastoma. Last but not least, I am very grateful to my family and friends for all the support.

List of abbreviations

ACC – accutase

APCs – antigen-presenting cells

Arg-1 – arginase-1

BBB – the blood-brain barrier

BMDM – bone marrow-derived monocytes/macrophages

BTD – Brain Tumor Dissociation kit

CAFs – cancer-associated fibroblasts

CCL2 – chemokine C-C motif ligand 2

CD – a cluster of differentiation

CNS – the central nervous system

CSCs – cancer stem cells

CTLA-4 – cytotoxic T lymphocyte-associated protein-4

DNA – deoxyribonucleic acid

DNAse – deoxyribonuclease

DMEM F12 – Dulbecco's modified eagle's medium F12

ECM – extracellular matrix

EDTA – ethylene diamine tetraacetic acid

FAP – fibroblast activation protein α

FBS – fetal bovine serum

FMO – fluorescence minus one control

FoxP3 – forkhead box P3

FSC – forward scatter parameter

GAMs – glioblastoma associated myeloid cells

GBM – glioblastoma

GITR – glucocorticoid-induced TNFR-related protein

IDH – isocitrate dehydrogenase

IFNγ – interferon γ

IL – interleukin

Ly6C – lymphocyte antigen 6C

MFI – mean fluorescence intensity

MHC – major histocompatibility complex

MDSCs – myeloid-derived suppressor cells

NK – natural killer cells

NKp46 – natural cytotoxicity triggering receptor 1

PBS – phosphate-buffered saline

PD-1 – programmed cell death 1

PD-L1 – programmed death-ligand 1

RPMI 1640 – Roswell Park Memorial Institute 1640 Medium

SD – standard deviation

SSC – side scatter parameter

STAT3 – signal transducer and activator of transcription 3

TGF-beta – transforming growth factor-beta

TILs – tumor-infiltrating lymphocytes

TNFα – tumor necrosis factor α

TMEM119 – transmembrane protein 119

Trypsin-EDTA – Trypsin-ethylenediaminetetraacetic acid

TDK – Tumor Dissociation kit

Treg – regulatory T cells

VEGF – vascular endothelial growth factor

WT – wild type

Abstract

Glioblastomas (GBMs) are one of the most common malignant tumors in the central nervous system. The tumor microenvironment of GBMs contains malignant and non-malignant stromal cells, whose interactions contribute to several GBMs characteristics, including aberrant angiogenesis, high proliferation rate, and systemic and local immunosuppression.

Fibroblast activation protein α (FAP) is a membrane serine protease that is sparsely expressed in healthy tissues but is upregulated in solid tumors, including GBMs. FAP can be expressed by both malignant and non- malignant stromal cells in the tumor microenvironment, and its expression in stromal cells has frequently been linked to impaired anti-tumor immune response. The role of FAP and FAP expressing stromal cells in the infiltration of immune subpopulations into the GBM microenvironment is still unclear. This diploma thesis aimed to develop a flow cytometry protocol for the analysis of immune cell subpopulations present within the tumor microenvironment in wild-type and FAP knockout mouse syngeneic glioblastoma model.

Four methods combining mechanical and enzymatic dissociation were evaluated for their ability to preserve cell viability and expression of studied surface molecules using mouse non-tumorous and GBM tissue. The most suitable method for mouse GBM tissue dissociation utilized a dissociator and enzymatical digestion with the Tumor Dissociation kit. This method provided high viable cell yield with minimum modification of surface markers. Panels for flow cytometry measurement of immune subpopulations (myeloid cells, conventional T cells, regulatory T cells, and natural killer cells) were designed. A pilot flow cytometry analysis revealed high infiltration of leukocytes, dominantly myeloid cells, into the GBM microenvironment with statistically non-significant differences in the composition of intratumoral immune cells between wild-type and FAP knockout mice.

The optimized method will be applied to mouse models of astrocytic tumors for further phenotypic characterization of immune subpopulations present in the tumor microenvironment.

Keywords: Glioblastoma, Fibroblast activation protein, immunosuppression, the tumor microenvironment, dissociation of tissue, flow cytometry, a mouse model

Abstrakt

Glioblastomy (GBM) jsou jedním z nejčastějších maligních nádorů v centrální nervové soustavě. Mikroprostředí GBM obsahuje maligní a nemaligní stromální buňky, jejichž vzájemné interakce přispívají k řadě charakteristik GBM, včetně aberantní angiogeneze, vysoké rychlosti proliferace a systémové a lokální imunosuprese.

Fibroblastový aktivační protein α (FAP) je membránová serinová proteáza, která je minimálně exprimována ve zdravých tkáních, ale je upregulována u solidních nádorů, včetně GBM. FAP může být v nádorovém mikroprostředí exprimován maligními i stromálními buňkami, přičemž jeho exprese ve stromálních buňkách je často spojena s narušenou protinádorovou imunitní odpovědí. Význam FAP a FAP exprimujících stromálních buněk v infiltraci imunitních subpopulací do mikroprostředí GBM není jasný. Tato diplomová práce se zaměřila na vývoj postupu využívajíciho průtokovou cytometrii k identifikaci subpopulací imunitních buněk přítomných v nádorovem mikroprostředí v modelu syngenního glioblastomu u myší divokého kmene a myší s genovou inaktivací FAP.

Byly vyhodnoceny čtyři metody kombinující mechanickou a enzymatickou disociaci z hlediska jejich schopnosti zachovat životaschopnost buněk a expresi studovaných povrchových molekul s použitím nenádorové tkáně a tkáně myšího GBM. Jako nejvhodnější metodu pro disociaci tkáně myšího GBM jsme vyhodnotili metodu používajíci disociátor a enzymatické štěpení pomocí Tumor Tissue Disociation kit. Tato metoda poskytla vysoký výtěžek životaschopných buněk s minimální změnou povrchových markerů imunitních buněk. Byly navrženy panely pro cytometrické stanovení imunitních subpopulací (myeloidní buňky, konvenční T buňky, regulační T buňky, přirozené zabíječské buňky). Pilotní cytometrická analýza nádorů odhalila vysokou infiltraci leukocytů, převážně myeloidních buněk, v nádorovém mikroprostředí GBM se statisticky nevýznamnými rozdíly v zastoupení intratumorálních imunitních buněk u myší divokého kmene i u myší s genovou inaktivací FAP.

Zavedená metoda bude použita pro další fenotypovou charakterizaci imunitních subpopulací přítomných v nádorovém mikroprostředí v myších modelech astrocytárních nádorů.

Klíčová slova: Glioblastom, Fibroblastový aktivační protein, imunosuprese, nádorové mikroprostředí, disociace tkáně, průtoková cytometrie, myší model

Table of Contents

1. Glioblastomas

Glioblastomas (GBMs) belong to the most common malignant tumors in the central nervous system (CNS), classified as grade IV, according to The World Health Organization [1]. Furthermore, GBMs are one of the deadliest cancers with high tumor recurrence and strong resistance to therapeutics. The current therapy includes surgical resection following radio/chemotherapy, but the prognosis remains poor [1]. The median survival of GBM patients is only 14 months after diagnosis (Fig. 1) [2]. The global incidence of GBMs is less than 3 per 100,000 people, with men more commonly affected than women [3–5]. The etiology of GBMs remains unknown. Genetic predisposition has only been observed in 10 % of patients. Still, the development of GBMs is probably a result of multiple mutations in genes associated with deoxyribonucleic acid (DNA) damage repair [6,7].

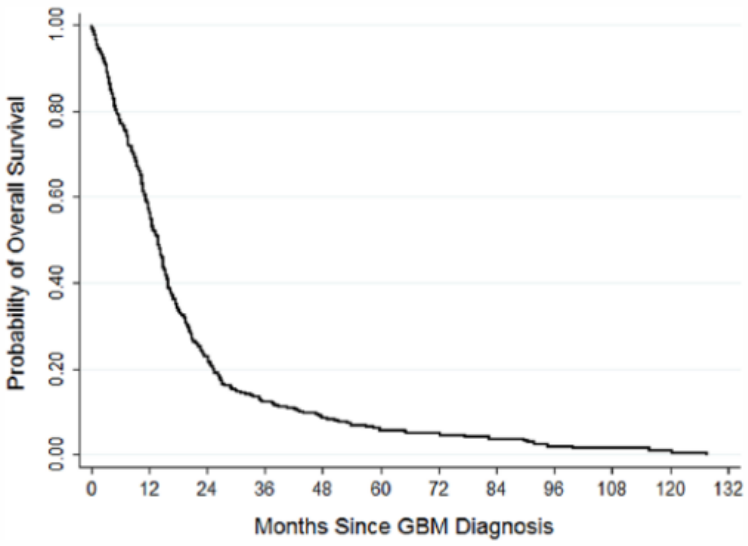

Figure 1: Kaplan–Meier survival curve of overall survival of glioblastoma patients

The curve represents the overall survival of patients after GBM diagnosis. The median survival of GBM patients is 14 months. Data were obtained from The Cancer Genome Atlas [2].

One of the possible origins of GBMs is astrocyte-like neural stem cells in subventricular zones [8]. Cancer stem cells (CSCs) are responsible for the initiation, maintenance, progression, and recurrence of the tumor [9]. The typical feature of CSCs is

genetic and phenotypical tumor heterogeneity. CSCs show variable expression of surface markers across GBM tumors [10].

GBMs are classified according to the mutations in isocitrate dehydrogenase (IDH) into GBM with wild-type IDH and GBM with mutated forms of IDH [1,11]. GBM, with wild-type IDH, developed *de novo* from the progenitor cells, is defined as primary GBM that accounts for approximately 90 % of all cases. GBM, with a mutated form of IDH, developed from pre-existing lower grade astrocytoma tumor, is defined as secondary GBM. GBM with a mutated form of IDH is a less aggressive form of cancer with a better prognosis [12].

Originally, GBMs were divided into neural, proneural, classical, and mesenchymal subtypes according to gene expression profile and characteristic genetic aberrations [13]. Transcriptomic analysis of GBM single cells revealed that neural subtype is non-tumor cell-related, and characteristic genetic features were enriched in proneural, classical, and mesenchymal subtype of GBM [14]. However, most GBM tumors may show gene expression profile characteristics of more than only one molecular subtype. Relapsed tumors have similar mutation patterns as paired primary tumors [15].

The response to treatment is affected by the particular subtype of GBMs [13]. The classical subtype is more sensitive to radio/chemotherapy; therefore, relapsed GBMs of the classical subtype are less frequent [13]. Proneural and mesenchymal subtypes are more frequently recurrent [16]. GBMs with mutated forms of IDH are almost invariably enriched in the proneural subtype [13].

GBM microenvironment consists of malignant and non-malignant stromal cells that interact through cell-cell contacts, soluble factors, and extracellular vesicles [17,18]. Complex interactions among stromal and tumor cells lead to immunosuppression in the tumor microenvironment.

1.1. Modulation of anti-tumor immunity in glioblastomas

For a long time, the brain was considered as an immune privileged organ lacking the cells of the lymphatic system. However, it was refuted by the visualization of a dural lymphatic vascular system in the mouse and human brain [19–22]. A dural lymphatic vascular

system drains immune cells and macromolecules from cerebrospinal fluid to the deep cervical lymph nodes to initiate an effective immune response [19,20,23].

The brain is protected from the infiltration of possible harmful neurotoxic molecules and pathogens by the blood-brain barrier (BBB). The BBB is a selective and semipermeable cellular border formed by brain endothelial cells, pericytes, and astrocytes. Hypoxic GBM microenvironment induces the impaired function of endothelial cells and pericytes, followed by disorganized blood vessels at the tumor site [24,25]. Abnormal formation of blood vessels is associated with disruption of BBB integrity [26]. The disruption of BBB and secretion of chemotactic molecules into the tumor microenvironment induce attraction of peripheral immune cell subpopulations such as bone marrow-derived monocytes/macrophages, regulatory T cells (Treg), conventional T cells and natural killer cells (NK) which interact with resident immune, stromal and tumor cells at the tumor site.

An anti-tumor immune response, including both adaptive and innate immune mechanisms, is responsible for the elimination of tumor cells. NK cells infiltrating into the tumor site recognize the abnormal expression of major histocompatibility complex (MHC) molecules, typical for various types of cancer, and mediate cytotoxic immune response by secretion of vesicles with perforin and granzyme [27]. A critical aspect of efficient anti-tumor immunity is the processing and presentation of tumor antigens by antigen-presenting cells (APCs). Microglia, the primary APCs in the brain, triggers T cell maturation into Th1 effector cells with a pro-inflammatory phenotype. $CD8^+$ T effector lymphocytes target malignant cells and provide a cytotoxic immune response. After the interaction of APCs and $CD4^+$ T effector lymphocytes, APCs become activated and more potent to phagocyte tumor cells. $CD4^+$ T effector lymphocytes interact with B lymphocytes that undergo somatic hypermutation. B lymphocytes produce specific antibodies binding tumor antigens, which improve the anti-tumor response [28]. However, tumor cells can develop various mechanisms to evade the anti-tumor immunity that lead to systemic and local immunosuppression.

GBM patients suffer from severe systemic immunosuppression. They have a lower total number of $CD4^+$ T cells in peripheral blood, compared to healthy donors, due to reduced T cell proliferation and sequestration of naïve T cells in bone marrow [29,30]. Moreover, the majority of $CD4^+$ T cells are Treg that produce anti-inflammatory

cytokines [29]. GBM patients have significantly reduced IL-2 and increased IL-10 in peripheral blood, which maintains Th2 anti-inflammatory, immune response [31]. Peripheral blood lymphocytes of GBM patients show a severe T cell exhaustion signature characterized by the upregulation of multiple immune checkpoint molecules [32]. Increased peripheral blood myeloid-derived suppressor cells (MDSCs) are linked to a worse survival outcome. GBM patients have a higher number of MDSCs in peripheral blood compared to other brain tumors [33]. GBM patients have several systemic immunosuppressive properties, but mechanisms of systemic immunosuppression have not been well elucidated.

In the tumor microenvironment, the immune cell subpopulations are either unable to detect and eliminate tumor cells or undergo apoptosis. Secretion of anti-inflammatory cytokines in the tumor microenvironment shifts phenotype of microglia towards tolerogenic M2 cells. Tumor cells are not effectively eliminated due to defective microglia phagocytosis. Microglia are unable to become functional APC cells; therefore, M2 microglia do not express co-stimulatory molecules essential for T cell activation. Furthermore, GBM cells express MHCI molecules normally and do not potentiate the activation and cytotoxic immune response of NK cells [34]. These cell interactions in the GBM microenvironment lead to the impaired local anti-tumor immune response.

1.1.1. Role of cell subpopulations in the glioblastoma immunosuppressive microenvironment

Tumor cells

Tumor cells produce transforming growth factor-beta (TGF-beta) and vascular endothelial growth factor (VEGF), which have various protumorigenic roles such as stimulation of tumor cell proliferation, induction of extracellular matrix (ECM) protein expression, or suppression of immune response [35,36]. Systemic depletion of TGF-beta reversed the immunosuppression in the tumor microenvironment to pro-inflammatory response and prolonged survival of tumor-bearing mice [37]. The production of VEGF by tumor cells enlarged tumor volume and reduced the infiltration of myeloid cells as a result of downregulated promigratory receptors and enhanced rate of cell apoptosis [38].

Additionally, the blockade of VEGF promoted the infiltration of antigen-presenting dendritic cells [39].

CSCs have lower expression of toll-like receptor-4 than surrounding cells; therefore, they are less sensitive to an innate anti-tumor response [40]. CSC-derived extracellular vesicles express programmed death-ligand 1 (PD-L1) [41]. PD-L1 is an immune checkpoint molecule binding to the PD-1 receptor expressed on activated T cells. PD-1/PD-L1 interaction in the tumor microenvironment suppresses the anti-tumor response of T cells [42].

PD-L1 can be taken up by myeloid cells as well, followed by their shift of phenotypic and functional properties towards the immunosuppressive M2 cells [41]. The blockade of PD-L1 molecule restored the activation of T cells [43]. GBM cell lines were seen to express Fas ligand [44,45]. Fas ligand binds to the Fas receptor expressed on activated T lymphocytes and promotes their apoptosis. However, Fas ligand expression has not been detected in GBM tissue yet.

Astrocytes

Astrocytes support endothelial cells that form the BBB, provide nutrition to neurons, and have a role in the repair and scarring process of the brain and spinal cord. In the tumor microenvironment, they become reactive astrocytes. Tumor-associated astrocytes express PD-L1 and promote suppression of T cell anti-tumor response. The astrocyte-microglia interaction induces secretion of TGF-beta and IL-10, followed by a shift in microglia and myeloid cell phenotype towards immunosuppressive M2 cells [46,47].

Myeloid cells

The GBM microenvironment consists of heterogeneous myeloid cell populations such as brain resident microglia and macrophages, together known as glioblastoma associated myeloid cells (GAMs), and MDSCs [48]. Resident microglia showed heterogeneity in phenotype dependent on the brain region [49]. Chemokine C-C motif ligand 2 (CCL2) is a critical chemoattractant and recruiting factor for Treg, and MDSCs produced mainly by GAMs [50]. Accumulation of GAMs in the tumor site was promoted by tumor secreted stroma-derived factor 1, macrophage colony-stimulating factor,

granulocyte-macrophage colony-stimulating factor, and epidermal growth factor [51,52]. GAMs undergo phenotypic polarization from pro-inflammatory M1 to anti-inflammatory M2 myeloid cells after exposure to glioblastoma derived factors, like IL-10, TGF-beta and highly express signal transducer and activator of transcription 3 (STAT3) [53]. GAMs promote invasive properties of tumor cells, support neovascularization, and contribute to immunosuppression in the tumor microenvironment. GAMs produced VEGF and stress-inducible protein 1, to enhance the recruitment of endothelial progenitor cells and invasion of GBM cells [54,55].

GBM induced expansion of MDSCs in the bone marrow and their attraction towards the tumor lesion [56]. The frequency of infiltrated myeloid cells is increased with tumor progression [57]. MDSCs are the primary source of Arginase-1 (Arg-1) in the tumor microenvironment responsible for the depletion of the amino acid L-arginine, which results in the suppression of T cells. The level of Arg-1 is elevated with tumor progression [57,58].

Tumor-infiltrating lymphocytes (TILs)

Tumor-infiltrating lymphocytes (TILs) consist of lymphocytic cells that invade the tumor tissue, predominantly $CD4^+$ and $CD8^+$ T cells, Treg, and NK cells.

The number of $CD8^+$ TILs was inversely, and $CD4^+$ TILs positively correlated with tumor grade, which indicates the unfavorable prognosis of GBM patients [59]. T cells showed predominantly effector memory phenotype rather than naïve phenotype, reflecting prior antigenic exposure. $CD8^+$ TILs in GBM tumors expressed multiple immune checkpoint molecules that demonstrate their exhaustion state. Dysfunctional state of $CD8^+$ TILs showed expression of PD-1 accompanied by TIM-3 and LAG-3 expression [32].

Treg constitutively expresses Glucocorticoid-induced TNFR-related protein (GITR), which is a co-stimulatory molecule. Anti-GITR antibodies significantly improved mice survival, elevated the pro-inflammatory activity of T cells, and induce the anti-tumor phenotype of macrophages [60]. Hypoxia-inducible factor 1α is an essential regulator of cellular metabolism in Treg. Hypoxia-inducible factor 1α switched glucose-based metabolism to fatty acids depended on mitochondrial metabolism. Treg with switched metabolism reduced the proliferation of $CD8^+$ T cells [61]. The direct

immunosuppressive mechanisms of Treg are mediated through the expression of cytotoxic T lymphocyte-associated protein-4 (CTLA-4) and PD-L1. The CTLA-4 interacts with costimulation molecules on myeloid cells and prevents the activation of T effector cells [62]. Indeed, CTLA-4 and PD-L1 blockade prolonged survival of mice bearing tumor [63,64]. The depletion of Treg in GBM inhibited the tumor growth [65].

Pericytes

Pericytes are contractile perivascular cells wrapping around the endothelial cells that line the capillaries and venules. Pericytes help to maintain BBB and brain homeostasis. Brain pericytes are part of the innate immune system and can behave as macrophage-like cells that possess phagocytic activity [66,67]. GBM cells induce immunomodulatory changes in pericytes in a cell interaction-dependent manner. Upon GBM interaction, pericytes showed lower phagocytic activity and decreased expression of the co-stimulatory molecules CD80 and CD86 and MHCII [67,68]. GBM associated pericytes secrete anti-inflammatory cytokines IL-10, TGF-beta, and are upregulated with PD-L1; therefore, they have impaired ability to activate T cells, unlike normal pericytes. Furthermore, pericytes negatively correlated with the presence of $CD8^+$ T cells [69].

Mesenchymal stem cells

Mesenchymal stem cells possess immunosuppressive properties and have been described in the GBM microenvironment. They express PD-L1 and secrete TGF-beta, CCL-2, IL-6, and VEGF to modulate the immune response. Moreover, this population of stromal cells induced the anti-inflammatory phenotype of myeloid cells [70].

2. Fibroblast activation protein

Proteases, in the context of the tumor microenvironment, have become a hotspot of recent studies [71]. In a variety of tumors, proteases are overexpressed and associated with protumorigenic actions like invasiveness of cancer cells, mesenchymal-epithelial transition, aberrant angiogenesis, and immunosuppression.

2.1. Structure

FAP is a type II cell-surface-bound transmembrane glycoprotein. In the genome, *FAP* is localized on chromosome 2. This gene encodes a 760 amino acid of transmembrane protein with six intracellular amino acids at the N-terminus, a 20 amino acid transmembrane region, and a 734 amino acid extracellular portion [72]. The protein has an enzymatically activated form after the dimerization of two monomers [73,74].

2.2. Enzymatic activity and substrates

FAP (also known as a serine prolyl endopeptidase and gelatinase) is a member of the peptidase S9b family. FAP possesses exopeptidase and endopeptidase activity. Enzymatic (aminopeptidase) activity is occurred by cleaving a specific N-terminal Xaa-(Pro/Ala) sequences (Fig. 2) [75]. Physiological substrates of FAP enzymatic activity are neuropeptide Y, B-type natriuretic peptide, peptide YY, incretins, substance P, glucagon-like peptide-1, glucose-dependent insulinotropic peptide and fibroblast growth factor 21 [76,77].

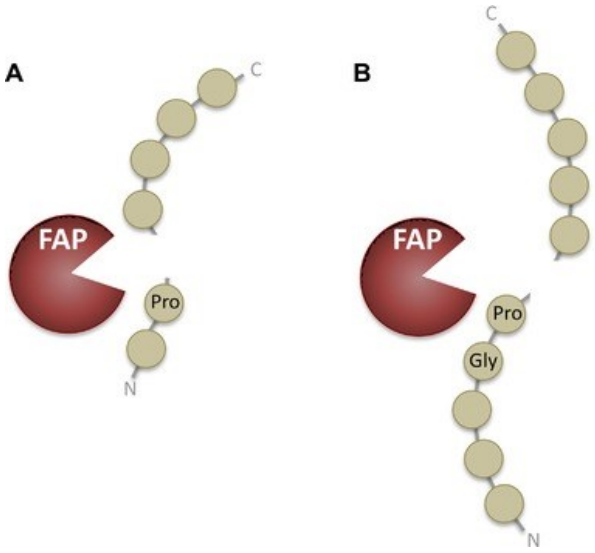

Figure 2: Enzymatic activity of FAP.

Schematic representation of FAP's (A) exopeptidase activity in the cleaving of N terminal peptide after proline residue and (B) endopeptidase activity restricted to the post-proline bond after glycine-proline sequence [75].

2.3. Expression and function

FAP is sparsely expressed in healthy tissues. However, human FAP expression was detected in pancreatic alpha cells, bone marrow, and uterine stroma [78–80]. Nevertheless, FAP expression is increased with malignant and non-malignant diseases during tissue remodeling.

The depletion of FAP^+ stromal cells in the C57BL/6J mouse model caused altered erythropoiesis and lymphopoiesis. Thus, it indicates the role of FAP in hematopoiesis in the bone marrow. Another study suggested that FAP deficiency did not cause any abnormalities in the number of immune cell populations in the thymus, lymph nodes, and spleen [81]. The loss of FAP^+ stromal cells was associated with reduced muscle loss and a cause of cachexia [82].

2.4. Fibroblast activation protein and immunosuppression in the tumor microenvironment

In the tumor microenvironment, FAP is expressed by malignant and non-malignant stromal cells, predominantly by cancer-associated fibroblasts (CAFs) [83,84].

In a transgenic mouse model with established immunogenic Lewis lung carcinoma, FAP expression was detected on both $CD45^-$ and $CD45^+$ cells. Depletion of tumor and stromal cells expressing FAP led to tumor shrinkage. However, the inhibition of FAP did not change the proportion of $CD4^+$, $CD8^+$, and forkhead box P3 ($FoxP3^+$) T cells. Furthermore, there was no change in the production of immunosuppressive cytokines IL-4, IL-10, IL-13, and TGF-beta. It was suggested that FAP^+ stromal cells either suppress the production of tumor necrosis factor α (TNFα) and interferon γ (IFN-γ) or attenuate cellular responses to these cytokines to protect the immunogenic tumor from cytokine-induced hypoxic necrosis [85].

Ablation of FAP expressing cells with both hematopoietic ($CD45^+$) or mesenchymal ($CD45^-$) origin led to a slower growth of tumor (established with Lewis lung carcinoma cells) compared to the control group which indicated that both cell populations are required for tumor progression. $CD45^+FAP^+$ cells were identified by flow cytometry as $F4/80^+$ macrophages with an M2 phenotype and represented approximately 10 % of all myeloid cells. $F4/80^+FAP^+$ macrophages were the primary source of heme-oxygenase-1 and promoted immunosuppression in the tumor microenvironment [86].

In ovarian carcinomas, FAP expression was positively correlated with the expression of FoxP3 and CD163, which indicated the role of FAP in the generation of cells with immunosuppressive properties at the tumor site. Furthermore, cells expressing FAP promoted the proliferation of tumor cells [87].

Mouse subcutaneously implanted with gastric cells and FAP^+CAFs had a reduced number of infiltrating T cells. Simultaneous blocking of FAP and PD-1 resulted in tumor growth arrest and prolonged mouse survival. Furthermore, inhibition of FAP and PD-1 increased the infiltration of $CD8^+$ T cells and reduced the number of Treg [88].

In a mouse intrahepatic cholangiocarcinoma model, the presence of CAFs expressing FAP caused decreased infiltration of $IFN\gamma^+CD8^+$ T cell but not $CD4^+$ T cells.

FAP$^+$CAFs were upregulated with STAT3 expression and were the primary source of CCL2 secretion, an important chemokine for MDSCs. Moreover, FAP$^+$CAFs induced expression of Arg-1 and nitric oxide synthase in MDSCs that became more effective in the inhibition of T cell proliferation [58]. Indeed, the depletion of FAP$^+$ stromal cells caused a reduced number of immunosuppressive myeloid cells and the expression of Arg-1 and nitric oxide synthase but did not affect the number of Treg. The depletion of FAP induced the anti-tumor immunity of CD8$^+$ T cells that started to produce IFNγ and TNFα. Simultaneously, PD-1 expression on CD8$^+$ T cells was significantly reduced. Besides, the production of Th2 related cytokines like TGF-beta and IL-10 was significantly decreased in the tumor microenvironment depleted with FAP [89].

Mesenchymal stem cells started to express FAP after exposure to esophageal squamous cell carcinoma and were defined as CAF-like cells. FAP expression by CAF-like cells induced a shift in macrophages towards the M2 phenotype. FAP$^+$CAF-like cells secreted CCL2, IL-6, and CXCL-8 to promote the migration of tumor cells and M2 macrophages [90]. FAP$^+$CAFs in oral squamous cell carcinoma promoted the generation of macrophages with M2 phenotype and induced their immunosuppressive properties by higher expression of Arg-1, IL-10, and TGF-beta [91].

Heterogenous FAP$^+$ mesenchymal cell populations with functional differences were identified in the tumor tissue of breast cancer. FAP$^+$ mesenchymal cells, which were also positive for podoplanin, had stronger immunosuppressive properties. FAP$^+$podoplanin$^+$ mesenchymal cells were responsible for the suppression of T cell proliferation by the production of nitric oxide in mouse breast cancer, similar to fibroblast reticular cells expressing FAP [92,93].

Interestingly, CAFs with upregulated FAP were more potent to have immunosuppressive properties and more aggressive protumorigenic behavior [58,94,95]. The presence of the cell population with the same origin but different functional properties determined by FAP expression indicates that immunosuppressive features of the tumor microenvironment might be conditioned by FAP expression and not by the particular cell subpopulation.

However, FAP in the tumor microenvironment of various solid tumors is expressed predominantly by CAFs, yet they were not detected in GBMs. On the other

hand, some of the stromal cell subsets in the GBM microenvironment share similar phenotypic and functional properties similar to CAF expressing FAP [84,96].

2.5. Fibroblast activation protein and glioblastomas

FAP is upregulated in GBMs compared to non-tumorous brain tissue. In GBMs, FAP is expressed by both tumor and mesenchymal stromal cells. [84,97].

The expression of FAP is associated with the mesenchymal subtype of GBM (data obtained from The Cancer Genome Atlas) [84]. Transcriptomic and multi-omic analysis of GBMs showed that mesenchymal subtype is associated with genes related to cell invasion and immune response. Furthermore, the mesenchymal subtype has a worse outcome compared to other molecular subtypes of GBMs [98]. The mesenchymal subtype is associated with increased genetic signature of tumor-associated M2 macrophages and reduced infiltration of activated NK cells compared to proneural and classical subtype [16]. Moreover, the mesenchymal subtype is associated with a worse prognosis [98–100].

3. Mouse model of glioblastomas

In vivo tumor model is commonly used for the study of the tumor microenvironment. There are several types of mouse models used in GBM studies, such as an immunocompromised model with xenografted human tumor cells, transgenic and spontaneous model, or immunocompetent syngeneic model [101]. Unlike human xenograft models, the syngeneic models do not require a deficient immune system. An immunocompetent syngeneic model offers an insight into tumor development as well as the host's immune response.

Mouse glioblastoma GL261 cells were induced by intracranial injection of 3-methyl-cholantrene into C57BL/6J mice [102]. The orthotopic transplantation of GL261 cells into C57BL/6J mouse offers efficient gliomagenesis, predictable, and reproducible growth rates and accurate knowledge of tumor location [103].

Brain tumors established from GL261 cells mimic many features of human GBMs. GL261 glioblastoma showed a non-metastatic growth pattern, similarly to its human counterpart. GL261 tumors exhibit poor cellular differentiation with atypical nuclei and multinucleated cells with a high proliferation rate [104]. The proliferation of intracranially implanted GL261 cells promoted the degradation of blood vessels and led to hypoxia with associated aberrant angiogenesis by secreted factors like VEGF-A and hypoxia-inducible factor 1 α, similarly to human GBMs [105].

Furthermore, GL261 tumors have a more detectable level of major MHCII than a healthy mouse brain, but there was no detection of MHCI similarly to human GBMs [34,104].

The applicability of the GL261 model in the research of the GBM immunosuppressive microenvironment is proven by its frequent use in preclinical studies of immunotherapeutic approaches for GBM treatment [106–109].

3.1. Mouse immune cell phenotyping for flow cytometry

Flow cytometry is a method that provides the analysis of a large number of cell subpopulations. Immune cell types can be distinguished by different marker expression (Tab. 1).

3.1.1. Myeloid cell populations

Brain myeloid cell populations consist of microglia, and BMDM infiltrated from the periphery. Microglia and BMDM represent two ontogenetically separate myeloid cell populations with different origin but similar immunomodulating functions. Microglia derive from the progenitors of the yolk sac in early embryogenesis and populate the brain parenchyma while BMDM arise from hematopoietic stem cells [110].

The primary immune cell population maintaining homeostasis in the CNS are microglia – resident myeloid cells exclusive for brain tissue. Under pathological conditions, microglia are activated and, together with infiltrated BMDM, restore the brain equilibrium [111].

In the healthy brain, the frequency of microglia is about 10–15% of all brain cells [112]. Microglia play a role in brain development and maintenance of physiological conditions of the neural environment. The primary role of microglia is the phagocytosis of apoptotic bodies and invading viruses or bacteria. Activated microglia become efficient APCs [113]. Post-inflammation microglia help repair damaged neural circuits and promoted the regrowth of neural tissue [114].

Both microglia and BMDM express receptor-type tyrosine-protein phosphatase C (CD45) but with a different intensity, which is used for the separation of resident microglia ($CD45^{low}$) from BMDM ($CD45^{high}$) [115]. Microglia can be distinguished from other myeloid cells by transmembrane protein 119 (TMEM119), which is a specific surface marker for brain resident myeloid cells [116].

Typical markers for pro-inflammatory M1 like myeloid cells are MHC class II antigen, CD11c, and CD11b. Tumor supportive M2 myeloid cells can be detected by the expression of the macrophage mannose receptor 1 (CD206) [117,118].

Three distinct $CD11b^{+}$ myeloid cells were identified, all of which were exclusive for the brain and were not observed in peripheral blood. CNS resident myeloid cells were positive for receptor-type tyrosine-protein phosphatase C (CD45) and bone marrow stromal antigen 2 (CD317) but differ by the expression of MHCII, ectonucleoside triphosphate diphosphohydrolase 2 (CD39) and T lymphocyte activation antigen CD86 (CD86). Simultaneously, they lack lymphoid marker T cell surface glycoprotein CD3 chains (CD3) (T cells), protein tyrosine phosphatase receptor type C (CD45R/B220) (B cells), Ly6C (monocytes) and lymphocyte antigen 6G (granulocytes) [119].

Levels of macrosialin (CD68) and MHCII significantly increased with age; on the other hand, the expression of F4/80 and CD11b do not change during lifetime [120].

3.1.2. Regulatory T cells

Treg are a cell fraction of $CD4^{+}$ T lymphocytes. Treg regulate immune response against both self and non-self antigens by the suppression of T effector cell activation and proliferation to prevent the development of various autoimmune diseases [131]. There are two populations of Treg: more frequent thymus-derived natural Treg (nTreg) and induced

Treg (iTreg) derived from peripheral naïve $CD4^+$ T cells [132]. In the healthy mouse brain, the number of Treg is low but increases in brain tumors [133]. During ischaemic brain injury, Treg suppress the inflammatory reactivity of astrocytes and potentiate neurological recovery [134].

Compared to other lymphocytes, Treg are characterized by higher expression of interleukin-2 receptor subunit α (IL-2Rα) [135]. IL-2 is essential for Treg development, proliferation, and function [136]. By the overexpression of IL-2Rα, Treg obtain IL-2 more avidly than other T cells and induce cytokine deprivation-mediated apoptosis of T cells [137].

Transcription factor FoxP3, a master regulator in the development and function of Treg, was considered to be a concrete Treg marker [138]. Attenuated expression of FoxP3 could result in Treg instability and alteration of their immunosuppressive function [139]. Activation of Treg could lead to the instability of FoxP3 expression and their reprogramming into conventional T cells. However, nTreg are more stable in FoxP3 expression than iTreg [140]. Markers FoxP3 and IL-2Rα were found to be expressed on Treg subsets but rarely expressed on conventional T cells [121].

Another transcription factor crucial for the immunosuppressive functional properties of Treg is Helios [141]. nTreg are positive for both FoxP3 and Helios, while iTreg lack Helios expression [123]. Treg that express Helios and FoxP3 simultaneously are responsible for the prevention of autoimmune response [142].

The percentage of Treg characterized as $CD4^+FoxP3^+$ cell population from all $CD4^+$ cells is approximately 17 % in lymph nodes and 10 % in a spleen. Treg cell populations in spleen and lymph nodes are more heterogeneous and numerous than in thymus, where they are barely detectable [126]. Some cell subsets were identified mostly based on L-selectin (CD62L) and lymphocyte antigen 6C (Ly6C) expression. Activated Treg express CD44 and display a low or absent expression of CD62L and Ly6C [124–126].

GITR, a co-stimulatory molecule, is essential for nTreg thymic development and expansion. On the other hand, the expression of GITR could result in the loss of FoxP3 expression, thus reducing Treg population [122,143]. Lower expression of GITR could be detected on naïve T cells as well and increases after their activation [144].

3.1.3. Natural killer cells

NK cells are a cell subpopulation originating from lymphoid lineage. They lack antigen-specific cell surface receptors and provide a rapid immune response without previous activation. They are essential in an immune response against pathogens and tumor cells and are usually the first effector cells at an inflammatory site. Through their activating and inhibitory receptors, NK cells are able to recognize stressed, and tumor cells with impaired MHC molecules expression [141]. NK cells are almost undetectable in the mouse brain under physiological conditions [146].

Splenic NK cells have a more reactive phenotype than NK cells in peripheral blood. In mice, two main subsets of NK cells were identified, referred to as NK1 or NK2 cells. NK1 cells are defined as CD27 antigen-negative α M (ITGAM) negative ($CD27^-$ $CD11b^+$) and NK2 as $CD27^+CD11b^-$ [127]. NK1 cells are preferentially recruited in the tumor microenvironment at early stages during tumor progression and neuroinflammation [128,147]. Brain-infiltrated NK cells showed a less reactive phenotype than splenic NK cells [128].

Natural cytotoxicity triggering receptor 1 (NKp46 or CD335) is expressed from immature to activating form of NK cells but is not expressed by natural killer T cells [129]. NK cells belong to Group 3 innate lymphoid cells; thus, they are negative for the CD3 marker.

Table 1: Overview of immune subpopulation phenotypes

Phenotype	Cell type		References
$CD4^+CD25^+$	- expressed by all Treg		[121]
$FoxP3^+$	- expressed by all Treg, not stable		[121,122]
$Helios^+$	- nTreg		[123]
$GITR^+$	- nTreg		[122]
$CD44^+Ly6C^-CD62L^-$	- the activated phenotype of Treg		[124–126]
$CD27^-CD11b^+$	- peripheral NK		[127]
$CD27^+CD11b^-$	- NK1 frequently occurred in the tumor microenvironment		[128]
$NKp46^+$	- expressed by all NK cells		[129]
CD45high	- BMDM		[115]
CD45low	- microglia		
$CD68^+$	- general markers for myeloid cells	- non-stable expression	[120]
$CD11b^+$		- stable expression	
$F4/80^+$		- stable expression	
$MHCII^+$, $CD86^+$	- M1		[130]
$CD206^+$	- M2		
$TMEM119^+$	- microglia		[116]
$CD317^+$	- microglia		[119]

4. Dissociation methods of tumor tissue for flow cytometry measurement

In order to acquire valid cytometry data, it is essential to choose the optimal dissociation method in order to have a proper single cell suspension (Tab. 2). Dissociation

of the tissue to single cell suspension can be done either enzymatically or non-enzymatically.

The main goal for preparing a single cell suspension from the solid tissue should be the preservation of cell viability and cellular diversity while maintaining qualitative and quantitative characteristics of cell population markers to provide the reliable cytometry data.

4.1. Non-enzymatic dissociation

Non-enzymatic tissue dissociation includes mechanical dissociation steps, like using strainers, tissue chopping, density gradient, trituration strategies, or using dissociator instruments without enzymatic digestion. However, using a non-enzymatic method could provide insufficient single cell suspension with cell aggregates and inconsistent cell yields [148]. The density gradient method by Percoll and Ficoll is commonly used for isolation of mononuclear cells but with lower cell yield than enzymatic dissociation [149–151]. On the other hand, the non-enzymatic method preserved the high viability of CD45 cells and did not alter the marker expression of immune cells after dissociation of tumor tissue [152].

4.2. Enzymatic dissociation

Selected enzymes should only digest proteins of ECM, proteins of cell-cell junctions, and DNA fragments released from dead cells without altering the expression of surface markers.

Papain

Papain is a cysteine protease that mainly digests proteins of cell-cell junctions. Papain was used for the isolation of human microglia, astrocytes for cell culture, and mouse medulloblastoma cells [153–155]. However, papain digestion leads to the contamination of cell suspension by DNA fragments released from lysed cells during an enzymatic breakdown, which results in the loss of viable cells [156–158].

Deoxyribonuclease

Deoxyribonuclease (DNAse) should also be included in the enzyme mixture due to its ability to prevent cell clustering via the degradation of DNA fragments released from dead cells [159].

Collagenase

Collagenase is sufficient for the degradation of peptide bonds in collagen, the protein of ECM. Collagenase has been used for the isolation of brain endothelial cells [160,161]. A combination of collagenase, hyaluronidase, and DNAse was used for the study of human brain tumor cells [156,162]. Despite the high viability of lymphocytes, the collagenase removed the CD4 surface marker [152].

Hyaluronidase

Hyaluronidase is an enzyme degrading hyaluronan, a structural proteoglycan in the ECM, and is standardly used in the mixture of enzymes with collagenase, DNAse, and neutral protease. This combination of enzymes was used in several studies associated with brain tissue dissociation. However, cell suspension treated with this mixture of enzymes has a high level of cell clumps, debris, and free DNA fragments [163].

Accutase

Accutase is a mixture of proteolytic and collagenolytic enzymes with DNAse activity, which preserves antigen expression and maintains intact cell morphology with high cell yield. The use of accutase alone is highly beneficial compared to the cocktail of several enzymes [164,165].

Tissue dissociation kit

Brain Tumor Dissociation kit (BTD) is suitable for the detection of cells in dissociated brain tumor tissue by flow cytometry. Tumor Dissociation kit (TDK) has a minimal digesting effect on the markers of immune cells isolated from tumor tissue[166,167].

4.3. Debris removal and erythrocyte lysis

Cell debris, dead cells, and erythrocytes provide high background during flow cytometry measurement and should be removed from the cell suspension. Cell debris and

clusters can be removed by a series of cell strainers and density gradient with Debris removal solutions. Commercially available lysing products to lyse erythrocytes differ in the mechanisms of the lysing process. We distinguish reagents with a fixative, which preserves leukocyte morphology and ammonium chloride-based reagents without a fixative.

Table 2: Overview of enzymes used for dissociation of brain and tumor tissue

Enzymes used in tissue dissociation	**Type of isolated cells**	**Pros**	**Cons**	**References**
Papain	microglia, astrocytes, tumor cells	digest proteins of cell-cell junctions	Loss of viable cells due to a lot of released DNA fragments	[153–156]
Collagenase, Hyaluronidase, Deoxyribonuclease	endothelial cells, tumor cells	degradation of ECM proteins, high viability of leukocytes	A loss of CD4 marker, high level of cell clumps a debris	[152,156,160–162]
Accutase	oligodendrocytes	a mixture of enzymes, preserves antigen expression, high viability of cells	none	[165]
TDK, BTD	myeloid cells, tumor-infiltrating lymphocytes	specifically developed for brain and tumor tissue	none	[166,167]

5. Aims of the thesis

Hypothesis

The presence of Fibroblast activation protein α (FAP) and stromal cells expressing FAP in glioblastoma is associated with local immunosuppression due to its effect on the specific composition of immune cells in the tumor microenvironment.

To identify immune cell subpopulations present in the tumor microenvironment, we have chosen flow cytometry as a tool of multiparametric analysis. For this purpose, we have set out the following aims:

Aim 1

Optimization of the dissociation method for mouse glioblastoma tissue to study infiltrated immune cells by flow cytometry analysis.

Aim 2

Flow cytometry analysis of immune cells (myeloid cell populations, conventional T cells, regulatory T cells, and natural killer cells) within the tumor microenvironment in a syngeneic glioblastoma model using wild-type and FAP knockout mice.

6. Materials and methods

6.1. Materials

6.1.1. Animals and cells

For all experiments, male mice C57BL/6J WT and C57BL/6 FAP-/-, 6-8 weeks old, and weighing 25 g were used. Experimental animals were kept in The Center for experimental biomodels at the 1st Faculty of Medicine, Charles University.

- Male mice C57BL/6J WT (The Jackson Laboratory United States of America) and male mice C57BL/6 FAP-/- (Boehringer Ingelheim Pharma Germany)
- Whole blood obtained from healthy mice C57 BL/6J WT
- Cells of Peritoneal lavage from healthy mice C57 BL/6J WT
- Splenocytes from healthy mice C57 BL/6J WT
- Brain tissue from healthy mice C57 BL/6J WT
- Brain tumor tissue from mice C57 BL/6J WT and C57 BL/6 FAP-/-
- GL261 cell line (Charles River Laboratories, United States), T98G, U373, U87, U138 (American Type Culture Collection, United States), U118 (Cell Lines Service GmbH, Germany), ZAM (cancer-associated fibroblasts derived from the skin metastasis of primary nodular melanoma, Department of Dermatovenerology, First Faculty of Medicine, Charles University) [168]

6.1.2. Chemicals

- 7-amino-4-methyl-coumarin (Sigma-Aldrich Chemie, Czech Republic)
- Accutase (Sigma-Aldrich Chemie, Czech Republic)
- Anesthetic mix: 1.5 ml ketamine (100 mg/ml) +1.2 ml xylazine (100 mg/ml) (both from Vetoquinol, Czech Republic) +7.3 ml 0.9% saline solution
- BD FACS™ Lysing Solution, (BD, United States of America)
- Cell wash (BD, United States of America)
- Coulter Isoton II Diluent (Beckman Coulter, United States of America)
- Debris Removal solution (Miltenyi Biotec GmbH, Germany)

- Dulbecco's modified eagle's medium F12 (DMEM F12) (Sigma-Aldrich Chemie, Czech Republic)
- Eosin (Sigma-Aldrich Chemie, Czech Republic)
- Ethanol 96%, 100% (obtained from Penta chemicals, Czech Republic)
- Fetal bovine serum (FBS) (Sigma-Aldrich Chemie, Czech Republic)
- Fc receptor blocking reagent, (Miltenyi Biotec GmbH, Germany)
- Foxp3/Transcription factor staining buffer (RD systems, United States of America)
- GlutaMAX (Thermo Fisher Scientific, United States of America)
- Hematoxylin (Sigma-Aldrich Chemie, Czech Republic)
- Hoechst 33258 (Sigma-Aldrich Chemie, Czech Republic)
- LIVE/DEAD™ Fixable Violet Kit (Invitrogen, United States of America)
- Ophthalmol-Azulen (Zentiva, Slovak Republic)
- Phosphate buffer (PBS) – 137 mM NaCl, 4 mM Na_2HPO_4, 2.68 mM KCl, 1.76 mM KH_2PO_4, pH 7.4 (Sigma-Aldrich Chemie, Czech Republic)
- Roswell Park Memorial Institute 1640 Medium (RPMI 1640 medium) (Sigma-Aldrich Chemie, Czech Republic)
- Trypsin-ethylenediaminetetraacetic acid (trypsin-EDTA) (Sigma-Aldrich Chemie, Czech Republic)
- Staining buffer (RD systems, United States of America)
- Tissue Freezing Medium (Jung, Germany)
- Tumor Dissociation Kit (Miltenyi Biotec GmbH, Germany)

6.1.3. Antibodies

The complete list of antibodies and their specific targets used in this study is shown in Tab. 3.

Table 3: Overview of used antibodies

Antibody target	Clone	Isotype	Fluorochrome	Manufacturer
CD45	EM-05	Rat IgG	PerCP	Exbio (Czech Republic)
CD3	145-2C11	Hamster IgG	PE-Cy7	
CD8a	53-6.7	Rat IgG2a kappa	PE	
CD4	GK1.5	Rat IgG2b	FITC	
CD335	29A1.4	Rat IgG2a kappa	PE	RD systems (United States of America)
F4/80	BM8	Rat IgG2a kappa	APC	
CD25	280406	Rat IgG2a	APC	
Helios	22F6	Hamster IgG	PE	(Miltenyi Biotec GmbH, Germany)

6.1.4. Laboratory equipment

- Autoclave SterilCave 18BDH (Cominox, Italy)
- BD FACS Verse (BD, United States of America)
- Centrifuges, Hettich Zentrifugen Universal 320R and Universal 16R (Hettich, Germany)
- Coulter Counter Z2 with 100 μm capillary (Beckman Coulter, Germany)
- CO_2 thermostat (Sanyo, Japan)
- Cryotome (Bright Instruments, United Kingdom)
- gentleMACS™ Dissociator, (Miltenyi Biotec GmbH, Germany)
- Hamilton Syringe (Hamilton Company, United States of America)
- KS 4000 ic control (IKA, Germany)
- Laminar Flow cabinet SafeFAST classic 212 (Faster Air, Italy)
- Microplate fluorimeter Infinite M1000 (Tecan, Austria)
- Microscope IX70 (Olympus, Japan)
- Pipetman Classic, P2, P10, P20, P100, P200, P1000 (Gilson, United States of America)
- Pump 11 Elite (Harvard Apparatus, United States of America)
- Stereotaxic device (Stoelting Co, United States of America)
- Surgical equipment (P-Lab, Czech Republic)
- Vortex-Genie2 (Scientific Industries, United States of America)
- Ultra-Turrax homogenizer fitted with an S8N-5G probe (IKA, Germany)

6.1.5. Laboratory consumables

- 96-well plates (Corning Costar, United States of America)
- Cell culture plastics (Nunc, Denmark)
- Chirlac braided violet HR22 EP3-USP2/0 1×70 cm (Harrmed Medical, CZ)
- Eppendorf tubes (Eppendorf, Germany)
- FACS tubes (BD, United States of America)
- Falcon tubes (Corning, United States of America)
- gentleMACS C Tubes (Miltenyi Biotec GmbH, Germany)
- Gilson tips (Gilson, France)

6.1.6. Software

- BD FACSuite™ software (BD, United States of America)
- Flow Jo v10.6.2 software (Flow Jo LLC, United States of America)
- ImageJ software (National Institute of Health, United States of America)
- QuickPHOTO MICRO 2.3 software (Promicra, Czech Republic)
- The Statistica 12 software (StatSoft, Inc., United States of America)

6.2. Methods

6.2.1. Cell culture

Cells were grown under standard cell culture conditions at 37 °C in the RPMI 1640 medium, supplemented with 10% fetal bovine serum (FBS), under a humidified atmosphere of 5% CO_2.

Cells were washed with 3 ml of PBS, and the supernatant was discarded. Then, the cells were added with 1 ml of Trypsin-ethylenediaminetetraacetic acid (Trypsin-EDTA) and incubated in the thermostat for 3 min at 37 °C. Enzymatic activity of Trypsin-EDTA was stopped by the addition of 4 ml of RPMI 1640 with 10% FBS and 1% GlutaMAX. The cells were transferred into a 15ml falcon tube and centrifuged at 250 g at 4 °C for 8 min. The supernatant was discarded, and the pellet of cells resuspended in 5 ml of RPMI 1640 medium. The cells were counted (*see 6.2.2.*), transferred into a 1.5ml eppendorf tube and centrifuged at 250 g at 4 °C for 8 min. The supernatant was discarded,

and the pellet resuspended in RPMI 1640 in concentration $2x10^6$/ml cells. The cells were distributed into aliquotes at 10 µl volume(one aliquot meant for one animal).

6.2.2. Cell counting

The cell suspension was diluted 1:200 (40 µl cell suspension in 8 ml of Coulter Isoton II Diluent) and counted by Coulter Counter Z2. Objects between 10 – 27 µm were counted.

6.2.3. Isolation of peritoneal macrophages

Mice were fully anesthetized and placed and fixed dorsally on the dissection table. A small incision was made in the center of the abdomen and firmly peeled the skin off to expose the peritoneal wall. The 20G needle was inserted into the peritoneal membrane to inject 10 ml of PBS into the peritoneal cavity. The abdomen was massaged for 10 – 15 seconds. Peritoneal fluid was carefully withdrawn, avoiding organs and fat, which could clog the needle. Peritoneal fluid was centrifuged at 250 g for 10 min at 4 °C. The supernatant was discarded, and the cell pellet was resuspended in 1 ml of Staining buffer prepared for staining.

6.2.4. Retro-orbital blood collection in mouse

A mouse was fully anesthetized. The mouse neck was gently scruffed, which made the eye bulge. A capillary tube with 20 µl of Trypsin-EDTA was inserted in the *venous sinus*. The blood was collected in the amount of 200 µl. Whole blood was resuspended in the Staining buffer and prepared for staining.

6.2.5. Stereotactic intracranial implantation

Mice were fully anesthetized with an intramuscular injection of an anesthetic mix before the surgery. The head was shaved, disinfected with Betadine, and a 5 mm incision was made longitudinally from the eye-level caudally for visualization of bregma. The mouse was placed on a stereotaxic device where its head was fitted into the adapter and fixed. The drill tip was placed over the bregma, and the drill tip was moved to a position 3 mm posterior and 2.5 mm lateral in the right cerebral hemisphere, and a 0.4 mm burr

pierced the skull. The GL261 cells were removed from the ice and gently resuspended. The cell suspension was slowly drawn by a 30-gauge flat bevel needle attached to a 10µl Hamilton syringe to avoid air bubbles into the volume of 6 µl. Then the drill was replaced by the Pump 11 Elite with attached Hamilton syringe. An alcohol pad was used to remove the cell suspension fluid from the tip of the needle to prevent contamination of the incision site with tumor cells, which could result in the extracranial tumor. The syringe was moved to the burr hole, maintaining the needle perpendicular to the skull. When the needle passed through the skull, the tip was slowly proceeding into the depth of 3 mm over 3 min.

The total volume of 5 µl (2000 cells/µl RPMI 1640) of GL261 cell suspension was injected in the posterior hippocampus over the time of 5 min (1µl/min) (Fig. 3). After injection of the cell suspension into the animal, the Hamilton syringe was left in the brain for 2 min and then slowly withdrawn over 3 min. After removing the Hamilton syringe, the burr hole was immediately covered by sterile bone wax. The edges of the incision were reapproximated with standard sewing atraumatic set [169]. All surgical interventions were done according to aseptic and antiseptic methods.

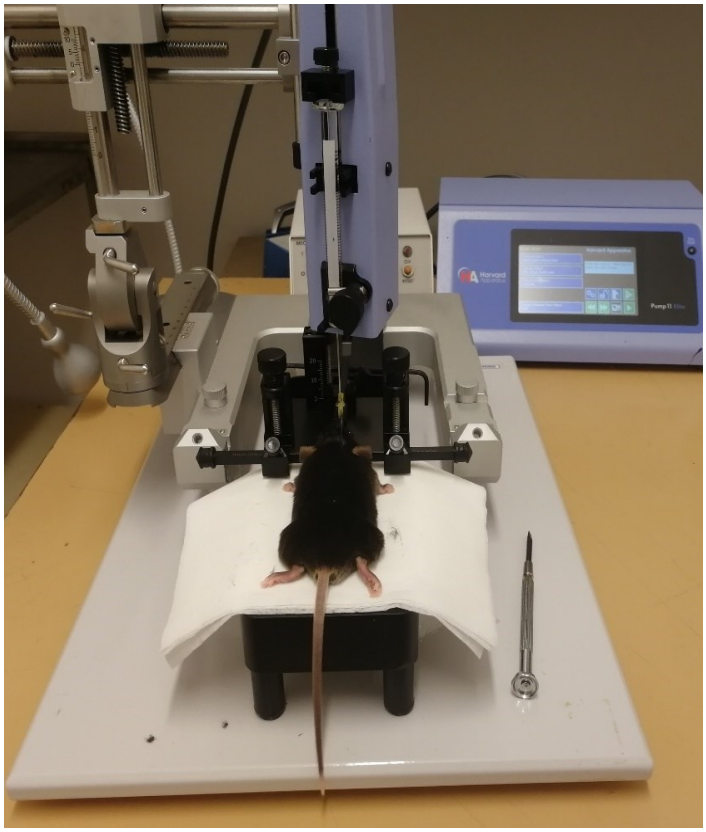

Figure 3: Stereotactic intracranial implantation

6.2.6. Mouse transcardial perfusion

Mice were fully anesthetized, placed, and fixed dorsally on the dissection board. By using iris scissors, a lateral incision was made through the abdominal wall and rib cage at both sides in a caudocranial direction to expose the liver and the heart. The transcardial perfusion method was done with a 10ml syringe with a 20G needle filled with 10 ml of PBS. The syringe was injected into the apex of the left ventricle, and the right atrium was incised with iris scissors. The transcardial perfusion was started immediately with a flow rate of 10 ml/min [170].

6.2.7. Hematoxylin-eosin staining

Brains were harvested and put into Tissue Freezing Medium. Frozen brains were stored at -70 °C. Serial frozen coronal sections 10 µm thick were cut using a cryotome at a temperature of –22 °C. Every fifth section was stained by hematoxylin and eosin and analyzed. Eosin was diluted in distilled water (1:20). The samples were fixed, rinsed, and stained according to Tab. 4. Quantification of the tumor size was done using the Cavalieri's method for unbiased volume estimation in ImageJ software with plugin Volumest [171].

Table 4: Hematoxylin and eosin staining

Fixation: 4 % paraformaldehyde	10 min
Rinse: dH2O	5 min
Staining: Hematoxylin	10 min
Rinse: H2O	10 min
Staining: Eosin	3 min
Rinse: Ethanol 60 %	3 min
Rinse: Ethanol 96 %	3 min
Rinse: Ethanol 100 %	3 min
Fixation: Xylene	3 min

6.2.8. Enzymatic activity measurement of Fibroblast activation protein

Tissue samples (brain, liver, kidney, lungs, muscle, spleen, pancreas) of one C57BL/6J WT and one C57BL/6 FAP-/- mouse and cell lines (T98G, U373, U87, U138, U118, ZAM, GL261) were lysed in ice-cold phosphate-buffered saline (PBS), pH 6.0, with a homogenizer fitted with an S8N-5G probe and used for enzymatic assay immediately.

Enzymatic activity of FAP in tissue samples was measured in polystyrene flat-bottom 96-well plates using a kinetic assay with 150 µm of N-(quinoline-4-carbonyl)-D-Ala-L-Pro-7-amido-4-methyl-coumarin as a fluorogenic FAP-specific substrate. FAP assays were done at 37°C in a total reaction volume of 100 µl in a PBS pH 7.5 buffer (8 mM NaH2PO4/42 mM Na2HPO4 – 150 mM NaCl). Fluorescence of the enzymatically released 7-amino-4-methyl-coumarin was measured on a microplate fluorimeter using excitation and emission wavelengths/slits of 380/5 nm and 460/5 nm, respectively. Measurements were performed in triplicate and calibrated with several concentrations of 7-amino-4-methyl-coumarin in the assay buffer.

6.2.9. Dissociation of tissue into single cell suspension

Tissue was dissociated by four different methods (Tab. 5) The tissue (spleen, right brain hemisphere) was cut into small 2–3 mm pieces in the Petri dish. 5 ml of DMEM F12 + 10% FBS was added to the minced tissue (method A) or 5 ml of accutase (method B) and incubated at 37 °C for 30 min. For methods C and D, minced tissue was transferred into tubes with 4.7 ml of DMEM F12, and Tumor Dissociation kit (TDK) (method C) or 5 ml of DMEM F12 + 10% FBS (method D). Minced tissue was dissociated by a gentleMACS™ Dissociator with program Brain_03 (60 s) followed with 30 min incubation at 37 °C. After the incubation, dissociated tissue was centrifuged at 161 g at 4 °C for 5 min.

Table 5: Methods for the dissociation of mouse tissue to detect immune cells by flow cytometry

A	B	C	D
Chopping		**gentleMACS™ Dissociator**	
DMEM F12+FBS	accutase	TDK	DMEM F12+FBS
Incubation	Incubation	Incubation	Incubation
Filtration	Filtration	Filtration	Filtration
Centrifugation	Centrifugation	Centrifugation	Centrifugation

6.2.10. Debris removal

Pellet of cells obtained after centrifugation of filtrated cell suspension was resuspended with 6.2 ml of PBS, and 1.8 ml of Debris Removal Solution was added. The suspension was mixed thoroughly. The suspension was overlayed very gently with 4 ml of PBS. The sample was centrifuged at 3000 g at 4 °C for 10 min with full acceleration and full brake. After centrifugation, three phases were formed, and the top 2 layers were very gently discarded. PBS was added to the volume of 15 ml, and the tube was spun upside down three times. The sample was centrifuged at 1000 g at 4 °C for 10 min. After centrifugation, the supernatant was discarded, and cells were ready for staining. The debris removal protocol was based on manufacturer instructions.

6.2.11. Lysis of erythrocytes

Erythrocytes in cell suspension were lysed by lysing solution, which was diluted 1:10 with distilled water. The volume of 3 ml of diluted lysing solution was added to 100 µl of cell suspension and incubated for 6 min at 4 °C. Erythrocytes were lysed under mild hypotonic conditions while leukocytes stayed preserved. The erythrocyte lysis protocol was based on manufacturer instructions.

6.2.12. Fc receptor blockade

Fc receptor is expressed on several subpopulations of immune cells and mesenchymal stem cells [172,173]. Fc receptor recognizes the Fc fragment of antibodies, which could lead to non-specific binding of antibodies and give false-positive results. Fc receptor blocking reagent blocks Fc receptors and decreases non-specific binding of antibodies. Fc receptor blocking reagent in the volume of 10 µl was added to 90 µl of cell

suspension and incubated for 10 min at 4 °C. After incubation, the sample was centrifuged at 161 g at 4 °C for 4 min, and the sample was ready for staining. The protocol for Fc receptor blocking was based on manufacturer instructions.

6.2.13. Flow cytometry data acquisition

Data for a flow cytometer BD FACS Verse were acquired by BD FACSuite™ software according to the parameters shown in Tab. 6.

Table 6: BD FACS Verse cytometer characteristics

Laser	Emission filter	Measured fluorochromes
Violet 405 nm	448/45	BD Horizon V450
	528/45	None
Blue 488 nm	488/15	None
	527/32	FITC
	585/42	PE
	700/54	PerCP
	783/56	PE-Cy7
Red 640 nm	660/10	APC
	783/56	None

Three panels were developed for the detection of immune subpopulations by flow cytometry (Tab. 7). Immune cells were identified by surface and intracellular positive and negative markers.

Table 7: Panels of antibodies for immune subpopulations detection

Panels	Cell populations	Markers	Fluorochrome
Panel 1	**T cells** ($CD45^+CD3^+CD4^+CD8^-$) ($CD45^+CD3^+CD4^-CD8^+$)	CD45	PerCP
		CD3	PE-Cy7
		CD8	PE
		CD4	FITC
	Myeloid cells ($CD45^+F4/80^+CD3^-$)	F4/80	APC
Panel 2	**NK cells** ($CD45^+CD3^-CD335^+$)	CD45	PerCP
		CD3	PE-Cy7
		CD335	PE
Panel 3	**Treg cells** ($CD4^+CD25^+Helios^+$)	CD4	FITC
		CD25	APC
		Helios	PE

6.2.14. Detection of dead cells for flow cytometry

The LIVE/DEAD™ Fixable Violet Dead Cell Stain was used to determine cell viability for flow cytometry by channel 448/45 and fluorochrome V450. The dye reacts with intracellular and extracellular amines. In the viable cells, the staining is limited only to extracellular amines. Cells with compromised membranes are also stained intracellularly, so they are more tend to bind a dye (Fig. 4). Dead cell control for gating strategy of viable brain cells and splenocytes was performed according to manufacturer instructions.

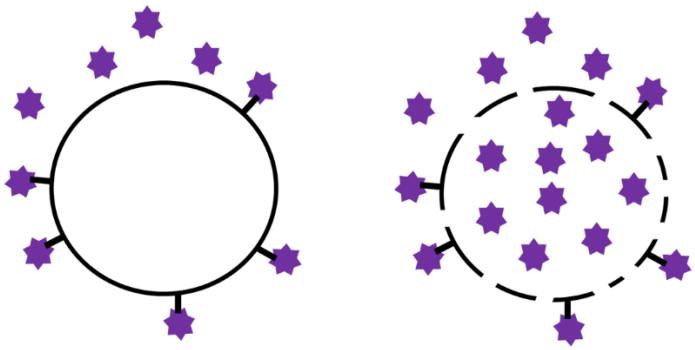

Figure 4: Staining of cells by LIVE/DEAD Fixable Violet Dead Cell Stain Kit

The dye binds primary amine groups of proteins. Living cells have only cell surface proteins labeled while dead cells allow the entry of the dye into the cytoplasm, and intracellular proteins are labeled as well.

6.2.15. Cell staining for flow cytometry

The samples of 50 µl of cell suspension were incubated for 30 min in the dark on ice with anti-CD45-PerCP, anti-CD3-PE-Cy7, anti-CD8a-PE, anti-CD4-FITC, anti-Helios-PE, anti-CD335-PE, anti-F4/80-APC, anti-CD25-APC and The LIVE/DEAD™ Fixable Violet Dead Cell Stain Kit. Commercial dye for dead cells was diluted 1000×. For intracellular staining, cells were fixed and permeabilized by Foxp3/Transcription factor staining buffer. The protocol for fixation and permeabilization was based on manufacturer instructions.

6.2.16. Titration of antibodies

Titration of antibodies was done on the mouse whole blood and peritoneal lavage. Whole blood was stained for extracellular markers (CD45, CD3, CD4, CD8, CD335). Peritoneal lavage was stained for an extracellular marker (F4/80). Antibodies for CD25 and Helios were used according to manufacturer instructions due to low levels of expression in the whole blood. All antibodies were diluted in PBS, whole blood, and peritoneal lavage was measured in the Staining buffer. Whole blood and peritoneal lavage were collected *(see 6.2.3., 6.2.4.)*. Serial dilution of individual antibodies was prepared in 10 µl of PBS, starting from the concentration recommended by the manufacturer (1:5) and then decreasing the concentration two-fold in each subsequent well until the final dilution of 1:640 in the final volume of 50 µl. Then, 50 µl of whole blood and peritoneal lavage were incubated with titrated antibodies for 30 min in the dark at room temperature. After 30 min, erythrocytes were lysed *(see 6.2.11)*. Next, the cells were washed by 1 ml of cell wash, centrifuged at 215 g for 5 min at 4 °C and immediately analyzed by a flow cytometer. The correct dilution of each antibody was chosen according to the mean fluorescence intensity (MFI) of both negative and positive populations, which were calculated by FlowJo. The measured MFI values are used to create the titration graph and calculate the stain index (Fig. 5). The stain index determines the optimal dilution by identifying the point of the best separation between positive and negative cell populations (Fig. 6).

$$\boldsymbol{Stain\ index} = \frac{MFI_{pos} - MFI_{neg}}{2\sigma_{neg}}$$

Figure 5: Calculation for the Stain index

The median fluorescence intensity of the negative population is subtracted from the median fluorescence intensity of the positive population, and the resulting number is divided by the standard deviation of the negative population times two.

A)

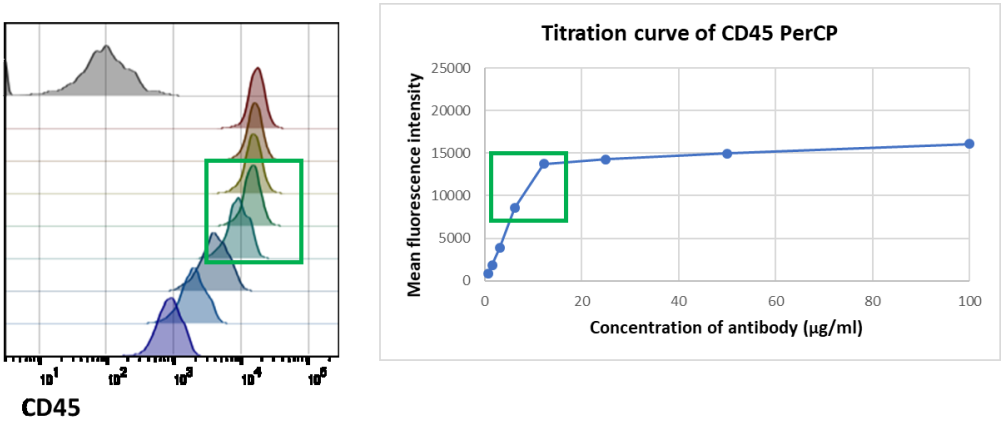
CD45
Titration curve of CD45 PerCP
Mean fluorescence intensity
25000
20000
15000
10000
5000
0
0
20
40
60
80
100
Concentration of antibody (µg/ml)

B)

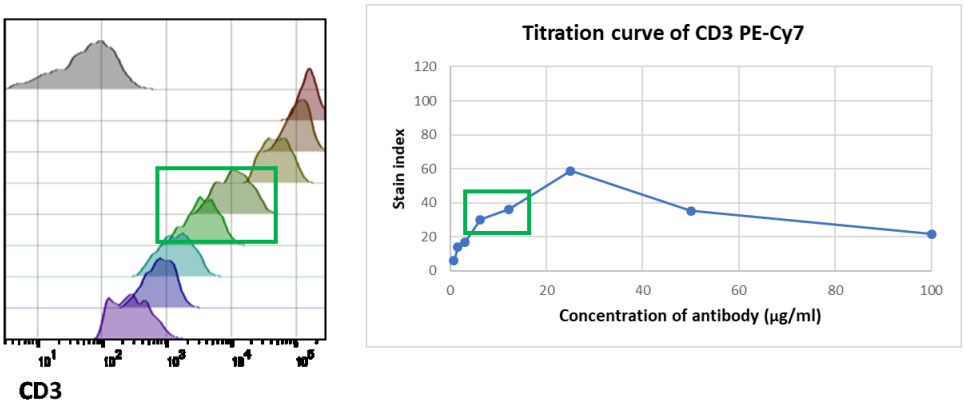
CD3
Titration curve of CD3 PE-Cy7
Stain index
120
100
80
60
40
20
0
0
20
40
60
80
100
Concentration of antibody (µg/ml)

C)

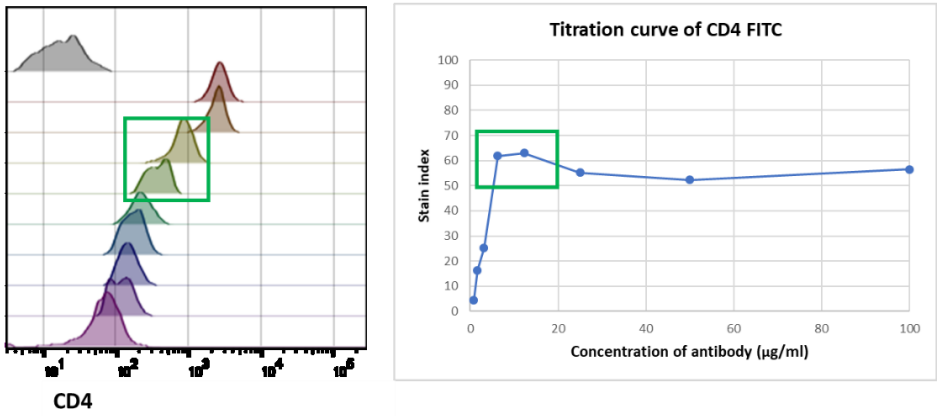
CD4
Titration curve of CD4 FITC
Stain index
100
90
80
70
60
50
40
30
20
10
0
0
20
40
60
80
100
Concentration of antibody (µg/ml)

D)

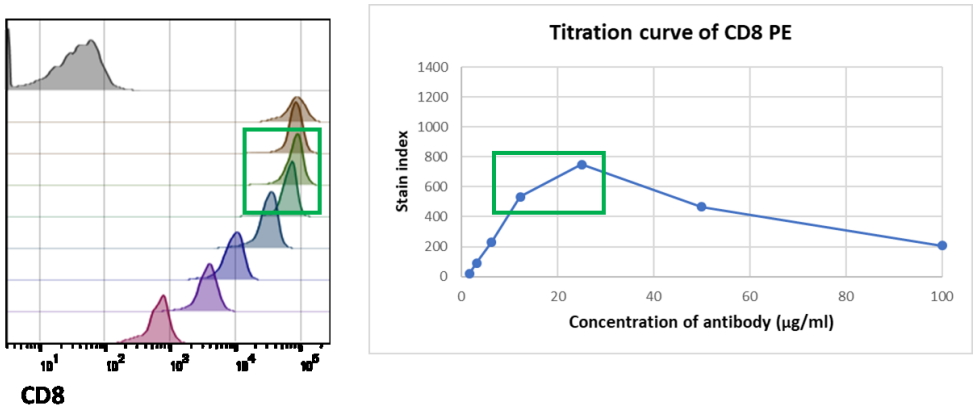

E)

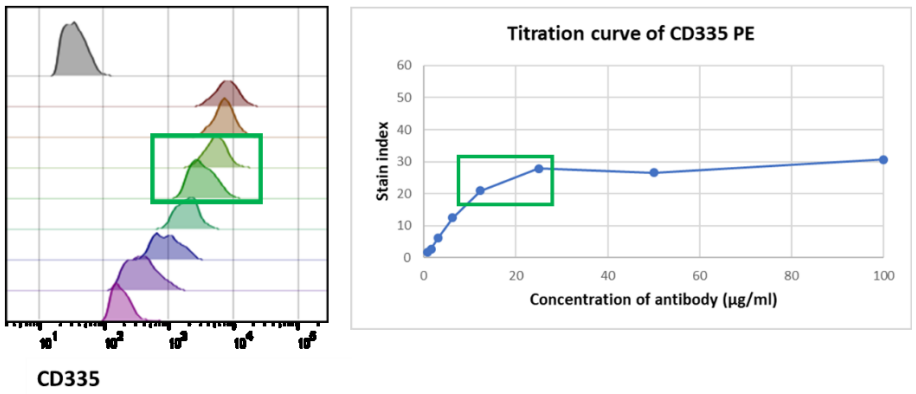

F)

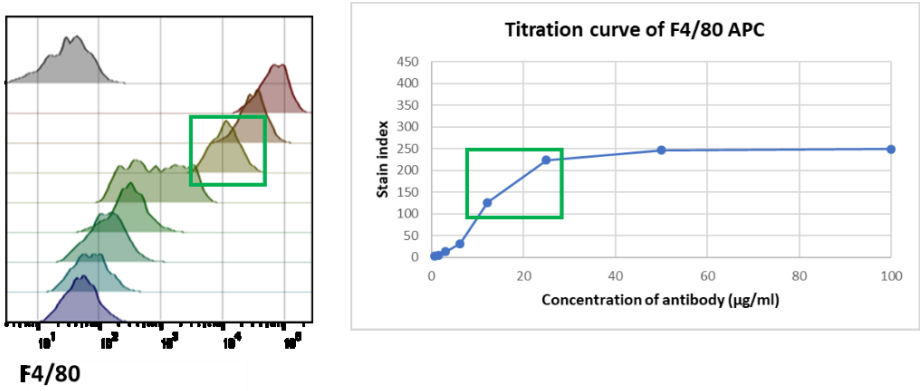

Figure 6: Histograms of expressed markers and titration curves of antibodies

Histograms of expressed markers (on the left) and titration curve (on the right) of diluted antibodies binding CD45 (A), CD3 (B), CD4 (C,) CD8 (D), CD335 (E), F4/80 (F). The histograms include unstained control (grey histograms) and positive cell populations. Each dot in the graphs of the titration curve represents one dilution in the serial dilution. The optimal antibody concentration is labeled in a green rectangle.

Table 8: Optimal concentration of antibodies

Antibody	Stain index/Mean fluorescence intensity	Dilution	The concentration of antibody (µg/ml)
CD45 PerCP	13720	1:40	12.5
CD3 PE-Cy7	36.2	1:40	12.5
CD4 FITC	61.8	1:80	6.25
CD8 PE	532	1:40	12.5
CD335 PE	20.9	1:40	12.5
F4/80 APC	223.9	1:20	25

6.2.17. Statistical Analysis

All statistical analyses were performed using Statistica 12 software, and value $p<0.05$ was considered statistically significant. Kruskal–Wallis and Mann Whitney U tests were used to determine the statistical significance of differences between groups.

7. Results

7.1. Design methods for dissociation of mouse glioblastoma tissue into a single cell suspension to detect immune cells

For valid cytometry data, it is crucial to have a proper single cell suspension. To obtain a single cell suspension from dissociated tissue, four dissociation methods were designed, based on studies that performed comparable processing of a brain or tumor tissue (Tab. 2). These methods included a combination of various non-enzymatic and enzymatic tissue dissociations.

Methods A and B involved dissection of tissue using a sterile scalpel. The minced tissue was non-enzymatically or enzymatically dissociated using cultivation medium with fetal bovine serum (DMEM+FBS) (A) or accutase (ACC, B), respectively. On the other hand, methods C or D included dissection of tissue using a gentleMACS™ Dissociator. The cell suspension was subsequently enzymatically digested in the Tumor Dissociation kit (TDK, C) or non-enzymatically triturated in DMEM+FBS (D). After incubation, the suspension was filtered through a 40 µm nylon mesh to remove undigested tissue residues (Fig. 7) *(see 6.2.9)*.

Each of the methods was evaluated for a viable leukocyte yield and modification of surface molecules. The quality of single cell suspension would be further improved by the removal of cell debris and lysis of erythrocytes.

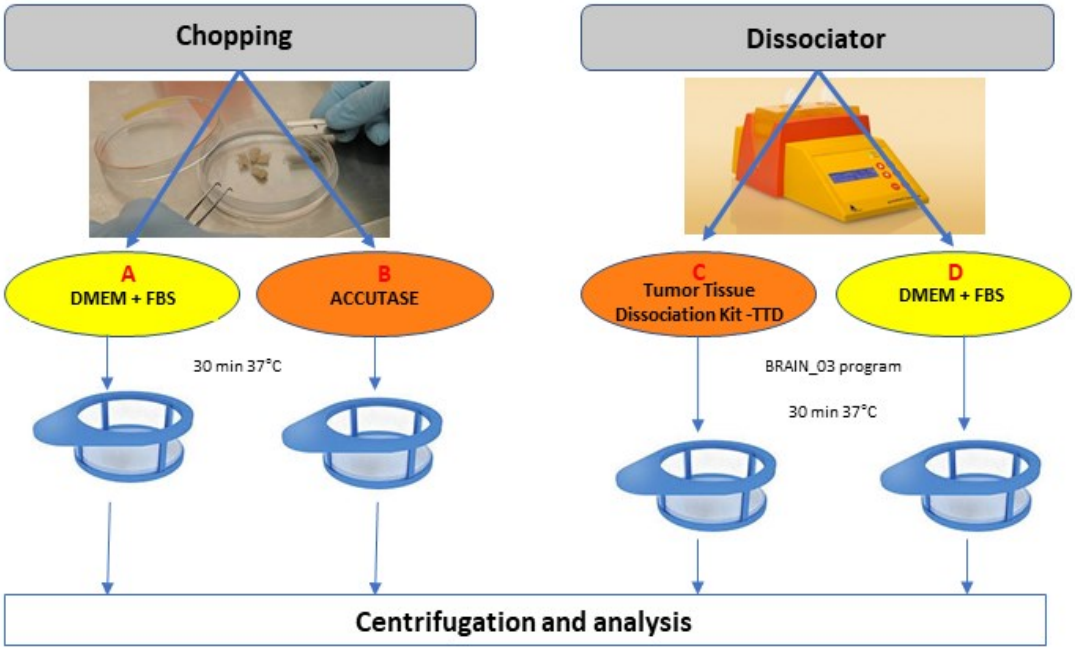

Figure 7: Overview of different protocols for the dissociation of mouse glioblastoma tissue for flow cytometry analysis

The tissue was mechanically dissociated in two ways using a scalpel or the dissociator. Methods A and B include tissue dissociation by chopping followed with either non-enzymatic (DMEM+FBS, method A) or enzymatic (Accutase, method B) treatment. Methods C and D include tissue dissociation by the dissociator, followed with either non-enzymatic (DMEM+FBS, method D) and enzymatic (TDK, method C) treatment. After dissociation, the cell suspensions were incubated for 30 min at 37 °C. Then, the cell suspensions were filtered through a 40 µm nylon mesh, centrifuged, and analyzed by flow cytometry.

Tumor Dissociation kit – TDK; DMEM+FBS - Dulbecco's modified eagle's medium F12+fetal bovine serum

7.1.1. Cell viability in cell suspension after dissociation of mouse tissue

Preparing a single cell suspension from solid tissue requires the degradation of ECM and cell-cell contacts, which may result in damaged cells and reduced cell viability. Glioblastoma tumors are typical for necrotic lesions that adversely affect cell viability. Therefore, potential dissociation methods were first applied to healthy tissue.

For this purpose, the effect of all four dissociation method on viable leukocyte yield was evaluated on the spleens of four healthy C57BL/6J mice. Harvested spleens were cut in three pieces (for technical triplicate), dissociated, and analyzed for each method.

Cell suspensions obtained from the dissociated spleens were stained for leukocyte marker CD45 (a universal marker of hematopoietic cells), cell viability, and measured by flow cytometry. The gating strategy excluded cell debris according to forward scatter vs. side scatter plot. Viable leukocyte yield was characterized as viable $CD45^+$ cells from all cells (Fig. 8A).

The lowest leukocyte viability (approximately 20 %) was observed in cell suspension obtained from spleen non-enzymatically dissociated by the dissociator. Slightly higher leukocyte viability was in cell suspension obtained from spleens dissociated using a scalpel followed with enzymatic or non-enzymatic treatment.

The highest viable $CD45^+$ leukocyte viability (almost 90 %) was detected in cell suspension obtained from the spleen dissociated using the dissociator and TDK (Fig. 8B).

A)

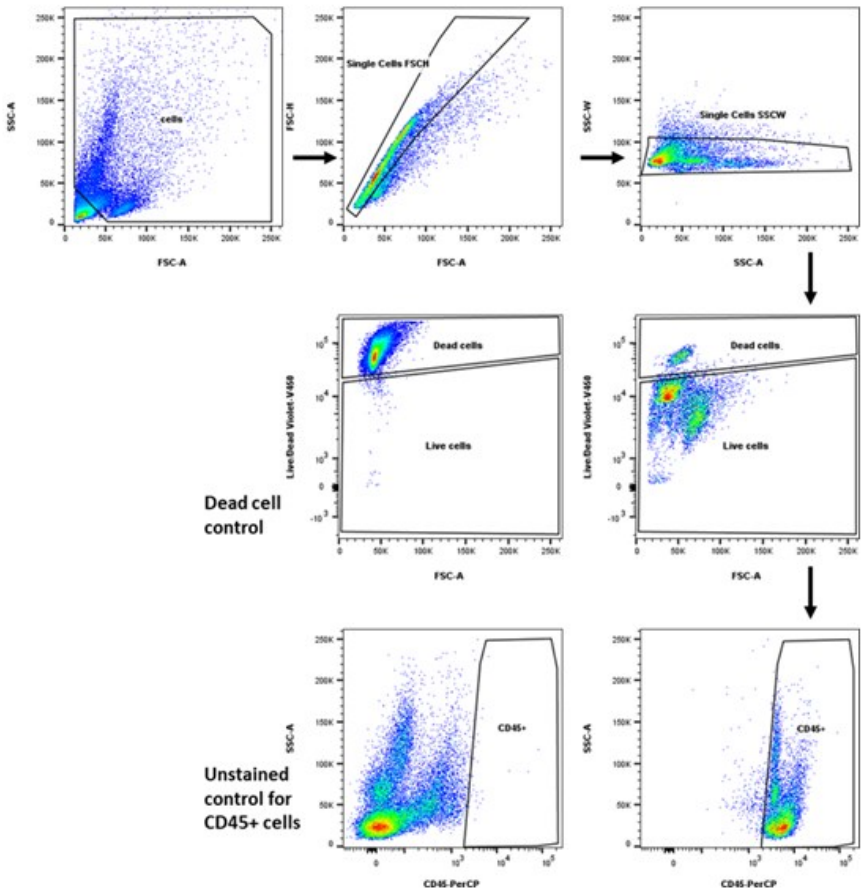
cells
Single Cells FSCH
Single Cells SSCW
Dead cells
Live cells
Dead cell control
CD45+
Unstained control for CD45+ cells

B)

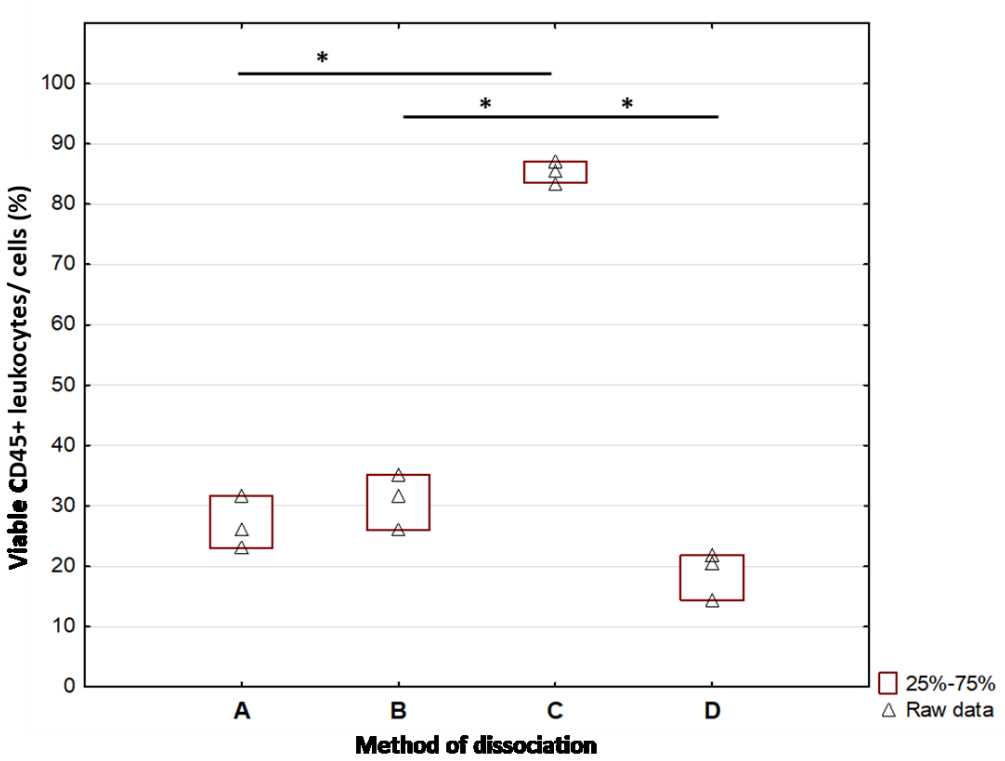

Figure 8: Viability of CD45$^+$ cells obtained from mouse spleen

A) *Representative gating strategy for viable CD45$^+$ leukocytes performed on the spleen of the healthy C57BL/6J mouse. Cells were gated based on their size and complexity according to FSC vs. SSC channels, and debris was excluded. Doublets discrimination was based on FSC-A vs. FSC-H and SSC-A vs. SSC-W. Gating strategy for viable and dead cells was performed according to dead cell control. CD45$^+$ leukocytes were identified according to unstained control.* ***B)*** *Viability of CD45$^+$ leukocytes in cell suspensions obtained from spleens of healthy C57BL/6J mice dissociated by methods A, B, C, or D; Boxes: middle 25-75% of measured values; triangles: raw data; three tissue pieces were dissociated and analyzed for each method; N=1 mice; *p<0.05, Kruskal–Wallis test*

After evaluating the viability of leukocytes in cell suspensions obtained from the dissociated spleens, the methods were applied on mouse GBM tissue to measure viable cell yield and infiltration of viable CD45$^+$ cells.

Four C57BL/6J mice were implanted intracranially with GL261 cells (one for each method) *(see 6.2.5)*. The highest viable cell yield in mouse GBM tissue, almost 70 % of all cells, was provided by the method using the dissociator and TDK. Similarly, the highest proportion of viable leukocytes obtained from mouse GBM was also provided by a method using the dissociator and TDK (Tab. 9).

Table 9: Proportion of viable cells obtained from mouse GBM

The percentage of viable cells and viable CD45$^+$ leukocytes in the mouse GBM tissue of C57 BL/6J dissociated by different protocols; N=1 mouse

Dissociation method	Viable cell yield in the mouse GBM tissue from all cells (%)	
	viable cells/ all cells	viable CD45$^+$ cells/ all cells
A (cut+DMEM+FBS)	50.2	6.49
B (cut+ACC)	43.1	12.5
C (dissociator+TDK)	69.4	35.8
D (dissociator+DMEM+FBS)	37.8	18.6

7.1.2. Surface marker expression on immune cells after enzymatic digestion

Enzymatic digestion of tissue could cleave a variety of cell surface molecules depending on the used enzymes. To determine the effect of enzymes on cell surface molecules crucial for further analysis - CD3, CD4, CD8, CD45, CD335 and F4/80, mouse body fluids (whole blood for lymphocyte markers, peritoneal fluid for myeloid cell marker) were enzymatically treated with ACC and TDK and compared to non-enzymatically treated samples. Marker CD25 was not tested due to low expression levels in whole blood and the necessity of fixation.

In the same way as tumor tissue, mouse body fluids were enzymatically treated for 30 min. The cleavage of cell surface markers was quantified by measuring the ratio of positive and negative mean fluorescent intensity (MFI) in samples treated with TDK, ACC, and non-treated samples. The surface marker expression in enzymatically treated samples was not significantly different compared to non-treated samples (Fig. 9).

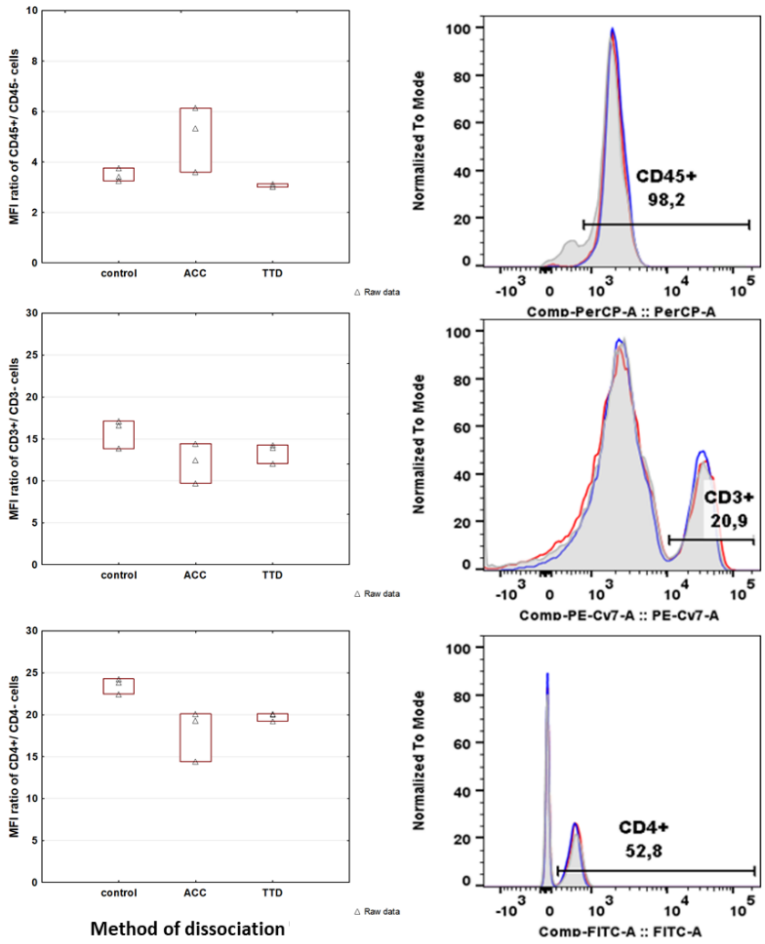
MFI ratio of CD45+/ CD45- cells
control
ACC
TTD
Raw data
Normalized To Mode
CD45+
98,2
Comp-PerCP-A :: PerCP-A
MFI ratio of CD3+/ CD3- cells
CD3+
20,9
Comp-PE-Cy7-A :: PE-Cy7-A
MFI ratio of CD4+/ CD4- cells
CD4+
52,8
Comp-FITC-A :: FITC-A
Method of dissociation

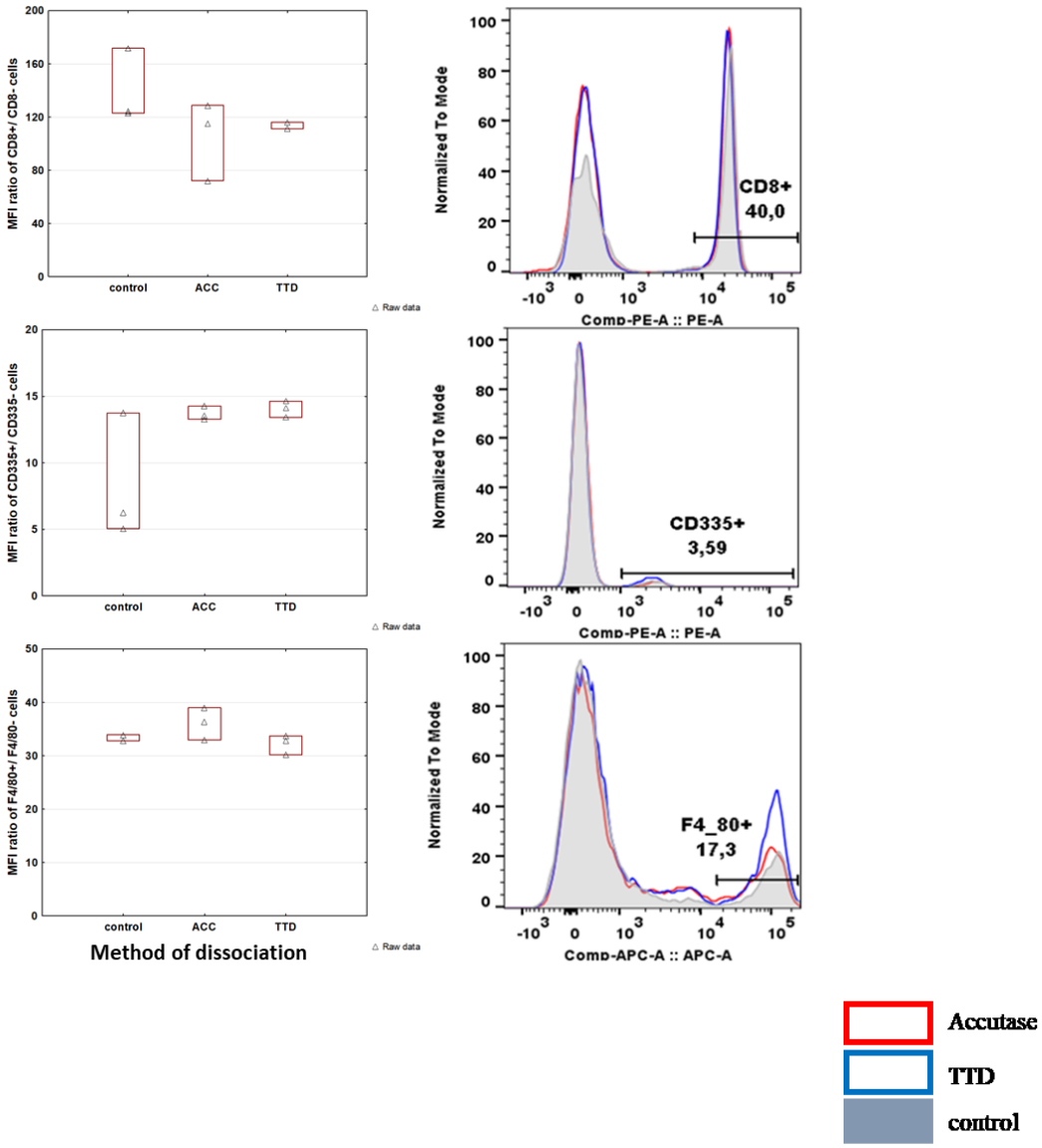

Figure 9: Surface marker expression in enzymatically treated whole blood and peritoneal lavage in comparison with non-treated samples

Surface marker expression in enzymatically treated samples of whole blood and peritoneal fluid by ACC and TDK was compared to non-treated samples. The results are shown as the ratio of positive and negative MFI in boxplots (left) and representative flow cytometry histograms (right), from top to bottom: CD45, CD3, CD4, CD8, CD335, F4/80. The experiment was performed in triplicate, raw data are shown by triangles; Kruskal–Wallis test CD45 (p=0.252); CD3 (p=0.288); CD4 (p=0.063); CD8 (p=0.193); CD335 (p=0.252); F4/80 (p=0.067). The relative counts shown in histograms for samples treated with ACC (red), TDK (blue), and control (grey) are normalized to one hundred.

ACC – accutase, TDK – tumor dissociation kit, control – non-treated samples, MFI – mean fluorescence intensity

7.1.3. Effect of debris removal on cell suspension quality

Mechanical dissociation and enzymatic digestion of the tissue along with preexisting necrotic lesions might cause cellular death resulting in cell aggregates. Cell debris and aggregates in cell suspension entail a problem in the analysis of flow cytometry data.

The effect of debris removal from cell suspension was evaluated on a healthy mouse brain sample *(see 6.2.10)*. The healthy brain was dissociated by a method using the dissociator and TDK (method C), which was previously evaluated to be the most suitable for glioblastoma tissue. The cell suspension was excluded from cell debris and analyzed by a light fluorescence microscope. The cell suspension was stained with Hoechst 33258 (green) either before (Fig. 10A) or after (Fig. 10C) cell debris exclusion. To verify that cells were not excluded as well, cell debris was stained with Hoechst 33258 (Fig. 10B).

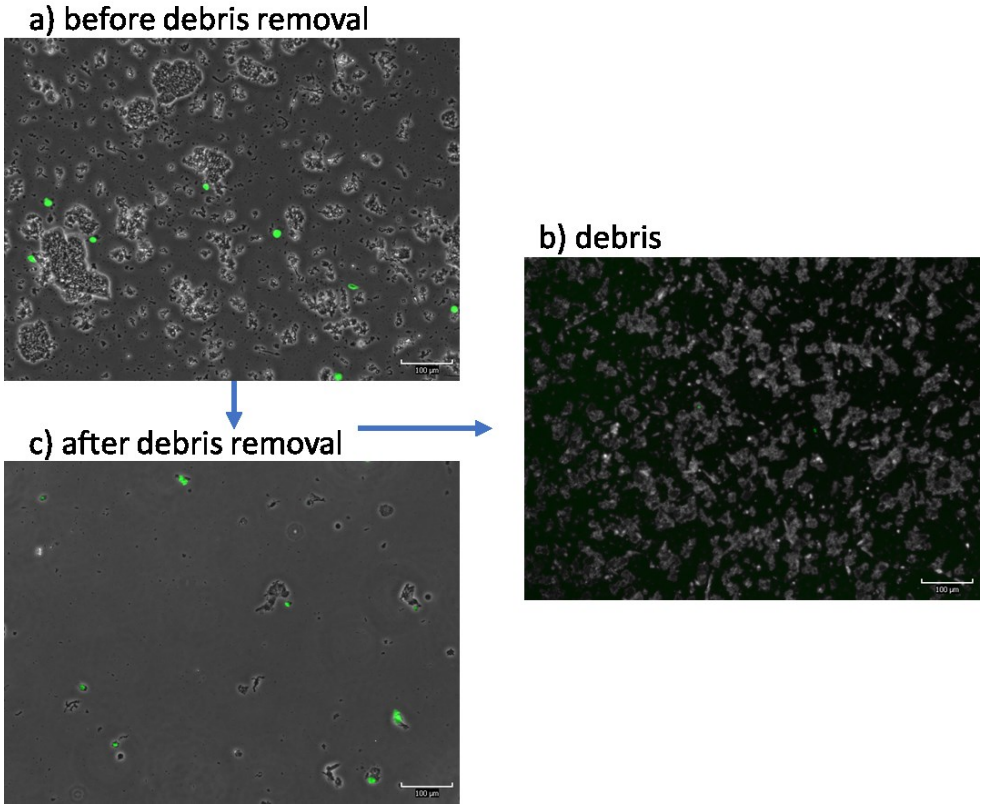

Figure 10: Removal of debris from cell suspension

Cell suspension before (a) and after (b) debris removal. The cell nuclei are stained with Hoechst 33258 (green). Scale bars represent 100 µm.

7.2. Gating strategy for immune cell populations in mouse glioblastoma

Gating strategies for immune cells were set on mouse GBM tissue. Viable leukocytes were identified with a common marker CD45. Two cell populations were identified among $CD45^+$ cells based on cell complexity as $CD45^+SSC^{high}$ and $CD45^+SSC^{low}$. $CD45^+SSC^{high}$ and $CD45^+SSC^{low}$ were considered to be myeloid cells and lymphocytes, respectively. Panel 1 was used for the detection of myeloid cells and conventional T cells. Myeloid cells were identified as $CD45^+F4/80^+$ and conventional T cells as either $CD45^+CD3^+CD4^+CD8^-$ or $CD45^+CD3^+CD4^-CD8^+$. (Fig. 11). In Panel 2, NK cells were identified as $CD45^+CD3^-CD335^+$ (Fig. 12). Panel 3 was used for the detection of Treg lymphocytes. For the identification of Treg, the cell suspension was fixed and permeabilized (*see 6.2.15*). Since $CD4^+$ lymphocytes represented a minor cell population in cell suspension, the viable cells were detected after the identification of $CD4^+$ cells. Treg were identified by surface marker expression - CD4 and CD25 markers and intracellular marker Helios (Fig. 13).

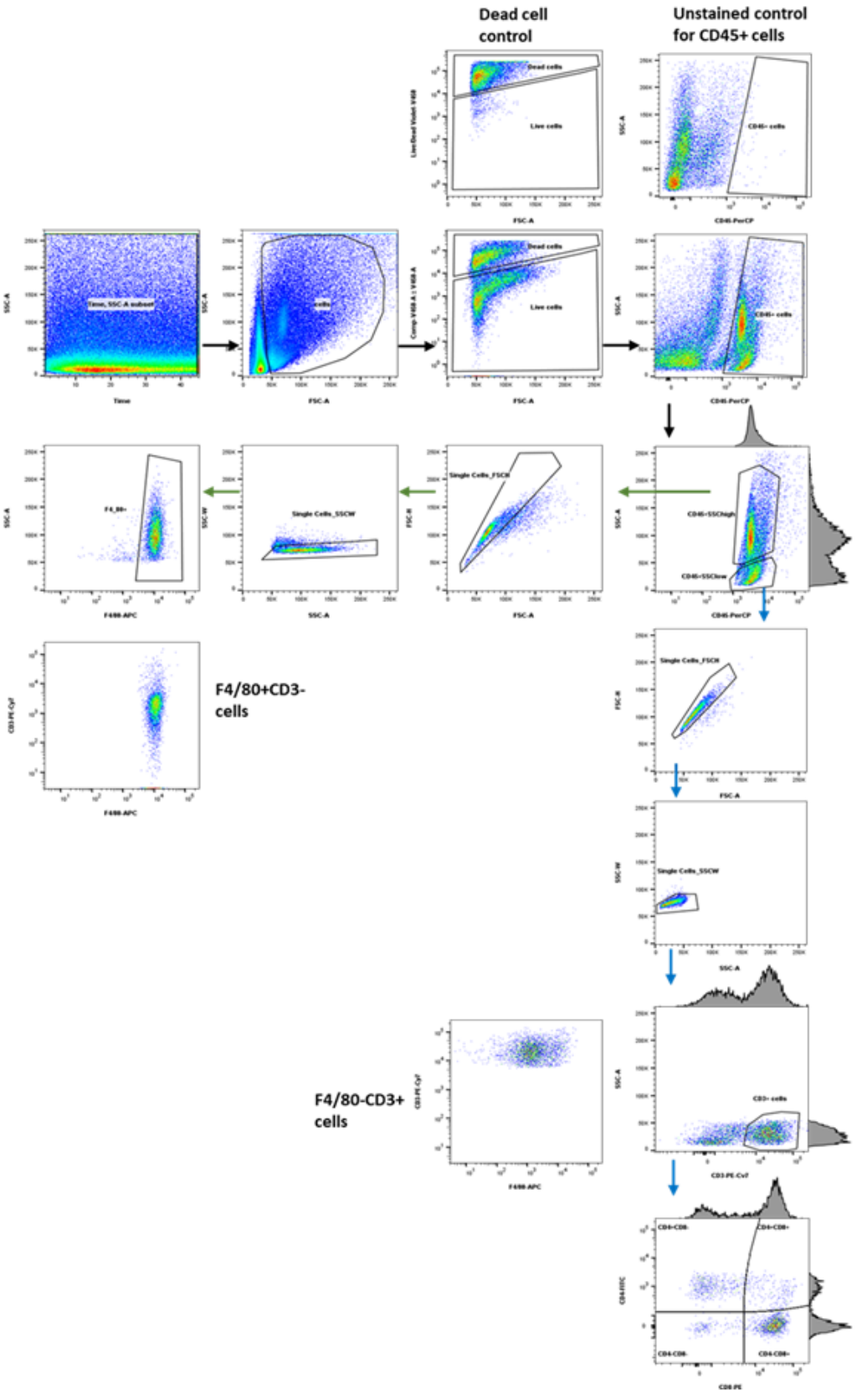
Dead cell control
Unstained control for CD45+ cells
Dead cells
Live cells
CD45+ cells
Time, SSC-A subset
cells
Single Cells_FSCH
Single Cells_SSCW
F4_80+
CD45+SSChigh
CD45+SSClow
F4/80+CD3- cells
F4/80-CD3+ cells
CD3+ cells
CD4+CD8-
CD4+CD8+
CD4-CD8-
CD4-CD8+

Figure 11: Gating strategy for myeloid and conventional T cells in mouse glioblastoma tissue (Panel 1)

Cells were gated based on their size and complexity according to FSC vs. SSC channels, and debris was excluded. Viable cells were identified according to dead cell control. Viable leukocytes (CD45$^+$ cells) were detected according to unstained control. Two cell populations were identified in CD45$^+$ cells based on complexity as CD45$^+$SSC^{high} (green arrows) and CD45$^+$SSC^{low} (blue arrows) and were analyzed separately. Single cells were identified by FSC-A vs. FSC-H and by SSC-A vs. SSC-W channels in both CD45$^+$ cell populations. CD45$^+$SSC^{high} were gated for F4/80$^+$ marker. CD45$^+$F4/80$^+$ cells presented as myeloid cells. Myeloid cells were negative for CD3 marker. CD45$^+$SSC^{low} cells were gated for the CD3 marker. Then, CD3$^+$ lymphocytes were gated for CD4 and CD8 marker. Conventional T cells had either CD45$^+$CD3$^+$CD4$^+$CD8$^-$ or CD45$^+$CD3$^+$CD4$^-$CD8$^+$ phenotype. CD3$^+$ lymphocytes were negative for F4/80 marker. Adjunct histograms were used for better visualization and resolution of positive and negative cell populations.

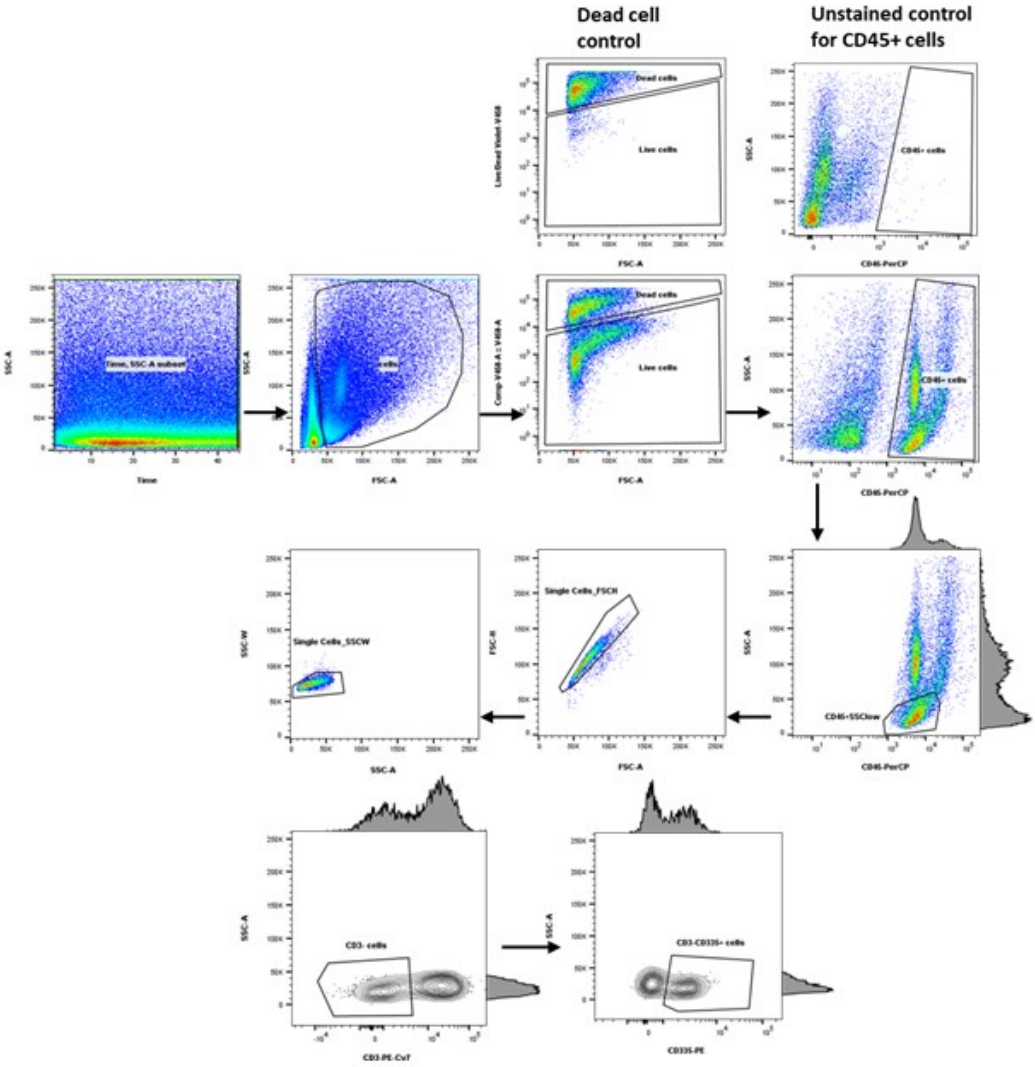
Dead cell control
Unstained control for CD45+ cells
Dead cells
Live cells
CD45+ cells
Time, SSC-A subset
cells
Single Cells_SSCW
Single Cells_FSCH
CD45+SSClow
CD3- cells
CD3-CD335+ cells
SSC-A
FSC-A
CD45-PerCP
Time
SSC-W
FSC-H
CD3-PE-Cy7
CD335-PE

Figure 12: Gating strategy for NK cells in mouse glioblastoma tissue (Panel 2)

Cells were gated based on their size and complexity according to FSC vs. SSC channels, and debris was excluded. Viable cells were identified according to dead cell control. Viable leukocytes (CD45+ cells) were detected according to unstained control. Lymphocytes were presented as $CD45^{+}SSC^{low}$ cells. Single cells were identified by FSC-A vs. FSC-H and by SSC-A vs. SSC-W channels in both $CD45^{+}$ cell populations. NK cells had $CD45^{+}CD335^{+}CD3^{-}$ phenotype. Contour plots and adjunct histograms were used for better visualization and resolution of positive and negative cell populations.

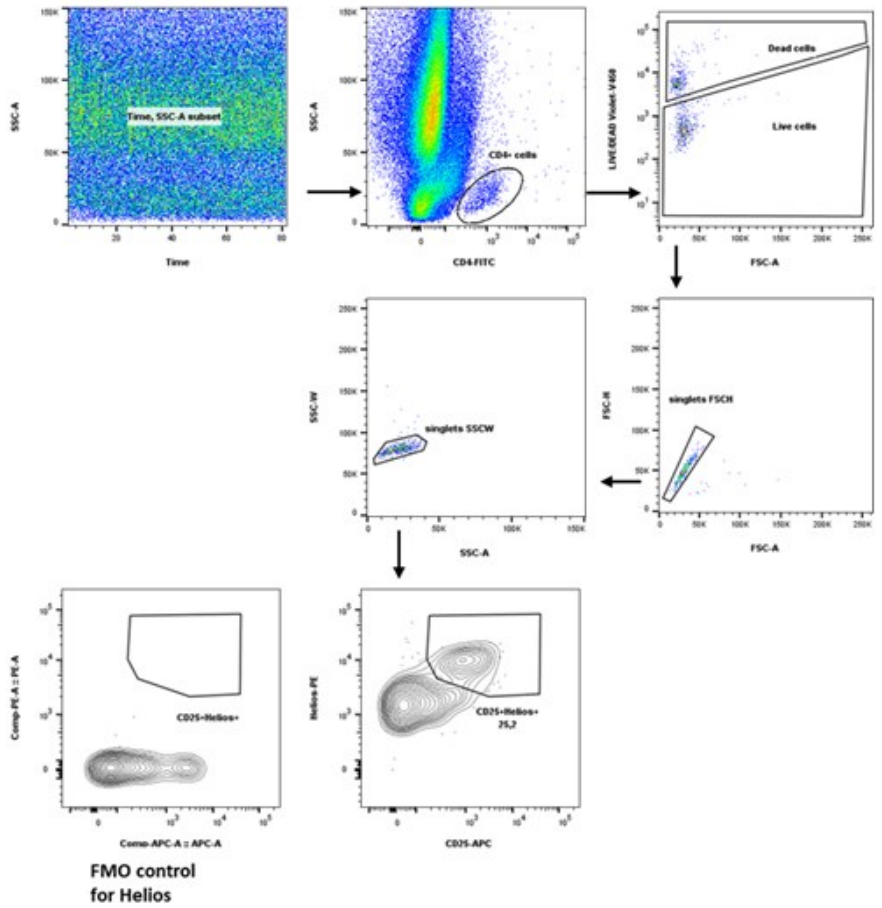

FMO control
for Helios

Figure 13: Gating strategy of Treg in mouse glioblastoma tissue (Panel 3)

$CD4^+$ lymphocytes were gated from all cells. Viable cells were gated after CD4 marker identification. Single cells were identified by FSC-A vs. FSC-H and by SSC-A vs. SSC-W channels. Treg were detected as $CD4^+CD25^+Helios^+$ cells. $Helios^+$ cells were identified according to FMO control for Helios marker. Contour plots have been used for better visualization and resolution of positive and negative cell populations.

FMO – fluorescence minus one

7.3. Characterization of an immunocompetent syngeneic mouse model of glioblastoma

Before analyzing how FAP expression influences the specific composition of immune cells in the tumor microenvironment, a syngeneic model of GBM in wild-type and FAP-/- mice was characterized.

First, FAP enzymatic activity was measured in GL261 cells and compared to human glioma cell lines expressing (U87, U138, U118) or not expressing FAP (T98G, U373), as well as to cancer-associated fibroblasts (ZAM) that are known for high FAP expression [174]. FAP enzymatic activity was hardly detectable in GL261 cells and was comparable to FAP enzymatic activity in human glioma cell lines not expressing FAP (Fig. 14A)

To confirm FAP deficiency in FAP-/- mice, FAP enzymatic activity was measured in harvested organs of C57BL/6 FAP-/- mouse and compared to organs of C57BL/6J WT mouse. FAP enzymatic activity was measured in brain, liver, kidney, lungs, muscle, spleen, and pancreas of healthy C57BL/6J WT and C57BL/6 FAP-/- mice. C57BL/6 FAP-/- mice had barely detectable FAP enzymatic activity in harvested organs. In C57BL/6J WT mice, the highest FAP enzymatic activity was measured in pancreas, liver, and muscle. FAP enzymatic activity in the brain was more than 2-fold lower compared to other harvested organs of C57BL/6J WT mice (Fig. 14B). FAP enzymatic activity was significantly higher in all harvested organs of C57BL/6J WT mice compared to C57BL/6 FAP-/- mice *(see 6.2.8)*.

To evaluate if tumor growth is affected by FAP expression in host cells in C57BL/6J WT and C57BL/6 FAP-/- mice, they were intracranially implanted with

GL261 cells. Tumors formed in both C57BL/6J WT and C57BL/6 FAP-/- mice. The brain tumors were harvested after four weeks. GBM tumors from both C57BL/6J WT and C57BL/6 FAP-/- mice were highly vascularized with wide necrotic areas and non-infiltrative tumor growth (Fig. 15A). Moreover, tumor volumes were not significantly different between C57BL/6J WT and C57BL/6 FAP-/- mice (Fig. 15B).

A)

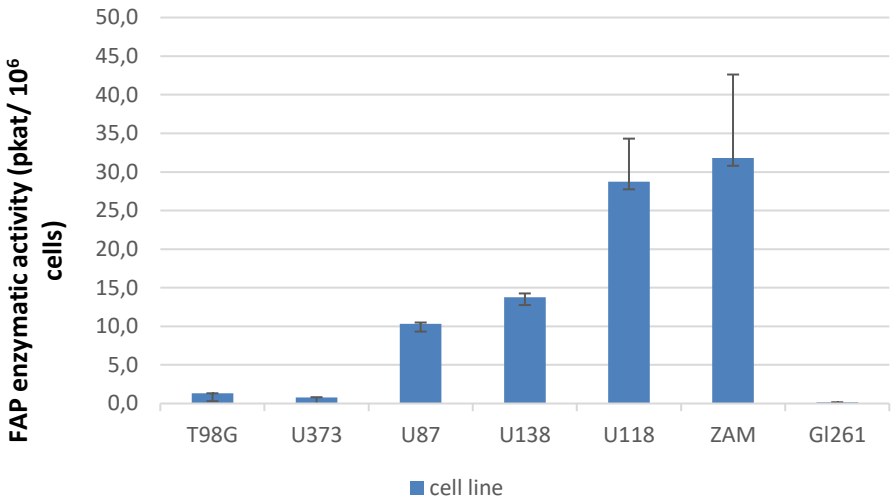

B)

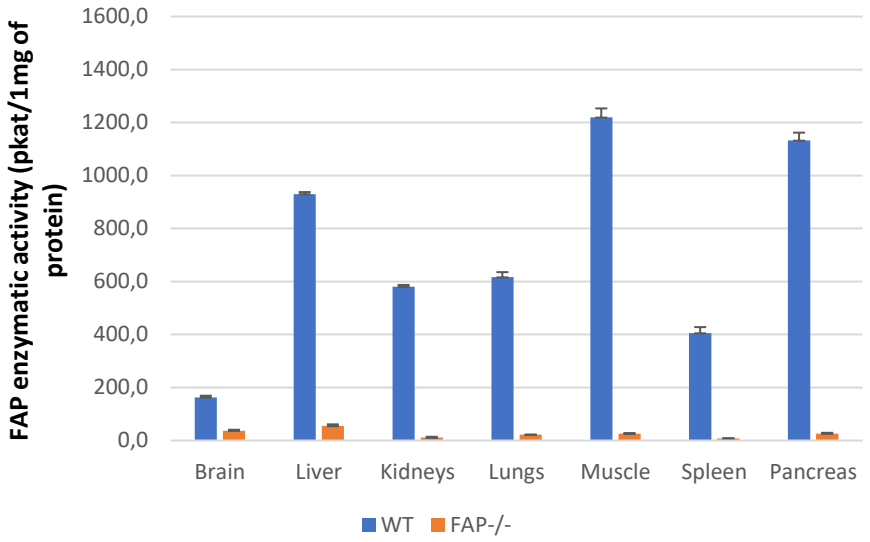

Figure 14: FAP enzymatic activity in organs of healthy C57BL/6J WT and C57BL/6 FAP-/- mice, human and mouse glioma cell lines and cancer-associated fibroblasts

A) FAP enzymatic activity (pkat/ 10^6 cells) determined in a panel of human glioma cell lines (T98G, U373, U87, U138, U118), cancer-associated fibroblasts (ZAM) and a mouse glioma cell line (GL261). ***B)*** *FAP enzymatic activity (pkat/1mg of total protein) in harvested organs (brain, liver, kidney, lungs, muscle, spleen, pancreas) of healthy C57BL/6J (blue) and C57BL/6 FAP-/- (orange) mice; N=1 mice*

A)

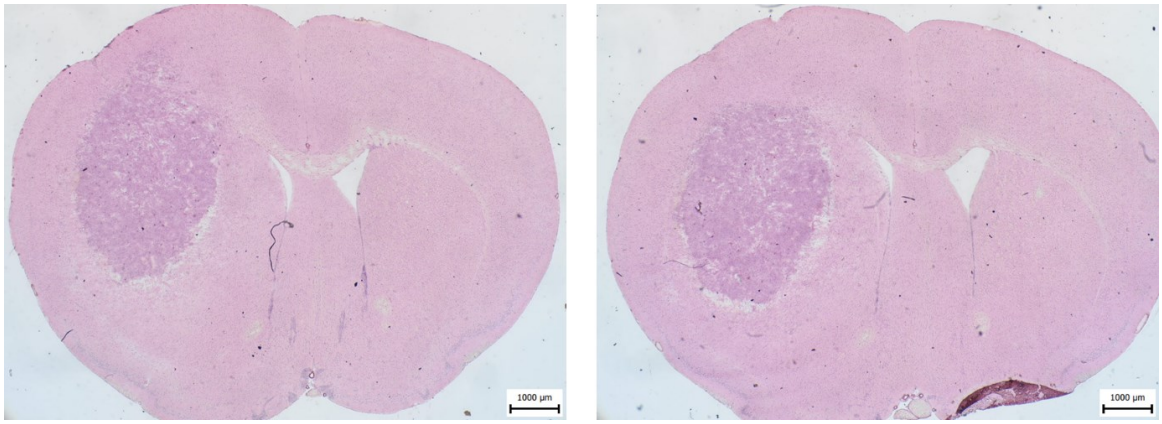

B)

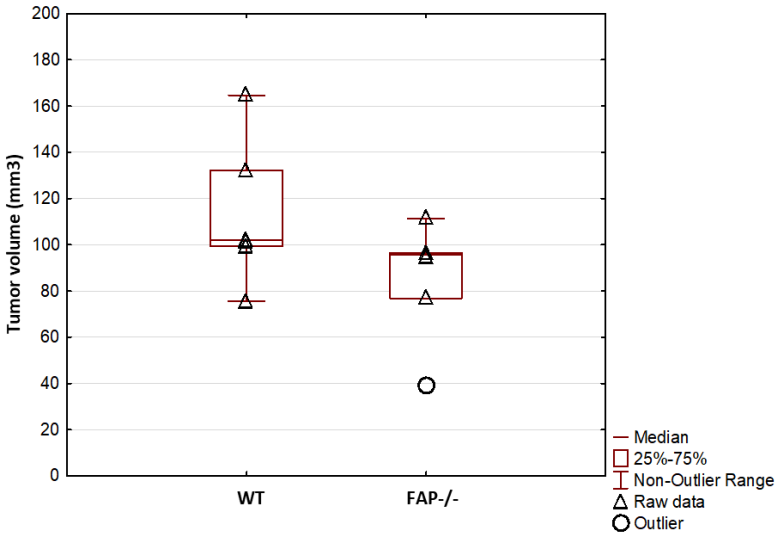

Figure 15: Tumorigenicity of GL261 cells in an orthotopic mouse glioblastoma model

A) Representative microscopy images of hematoxylin-eosin stained sections of mouse glioblastomas established by GL261 in the right brain hemisphere of C57BL/6J WT (left) and C57BL/6 FAP-/- (right) mouse. Scale bars represent 100 µm. ***B)*** *Tumor volume in C57BL/6J WT and C57BL/6 FAP-/- mice. Boxes: middle 25-75% of measured values; bars: non-outlier range; triangles: raw data; circles: outliers. There was no significant difference in tumor volume between C57BL/6J WT and C57BL/6 FAP-/- glioblastoma mouse model; N=6 mice; p=0.128; Mann Whitney U test*

7.4. Detection of immune cells in a syngeneic mouse model of glioblastoma in wild-type and FAP-/- mice

In order to determine whether the composition of immune cells in the tumor microenvironment is influenced by stromal FAP expression, immune subpopulations in the GBM microenvironment of C57BL/6J WT and C57BL/6 FAP-/- mice were analyzed. GL261 tumors from both C57BL/6J WT and C57BL/6 FAP-/- mice (three mice per group) were dissociated by an optimized method using the dissociator and TDK (method C). The viability of cells after tumor dissociation was more than 70 % in both C57BL/6J WT and C57BL/6 FAP-/- mice. The immune subsets were analyzed from all and viable cells and in the composition of viable leukocytes.

Leukocytes ($CD45^+$ cells) highly infiltrated into the GBM microenvironment, and their proportion was comparable in tumors in C57BL/6J WT and C57BL/6 FAP-/- mice (Fig. 16). Similarly, the proportion of individual immune subpopulations in the GBM microenvironment was not significantly different between C57BL/6J WT and C57BL/6 FAP-/- mice.

Myeloid cells representing approximately one-third of all cells were the major immune subpopulation in the GBM microenvironment in both C57BL/6J WT and C57BL/6 FAP-/- mice (Fig. 17, 20B).

The percentage of infiltrated NK cells in the tumor microenvironment were less than 5 % of all cells in both C57BL/6J WT, and C57BL/6 FAP-/- mice and represented the smaller fraction leukocytes (Fig. 18, 20B). The frequency of T cells was similar to the proportion of infiltrated NK cells in both C57BL/6J WT and C57BL/6 FAP-/- mice (Fig. 20B).

The proportion of $CD4^+$ T cells from all viable $CD3^+$ T cells was higher in C57BL/6J WT mice compared to C57BL/6 FAP-/- mice (Fig. 20A). Double negative T cells ($CD4^-CD8^-$) highly infiltrated the GBM microenvironment in both C57BL/6J WT and C57BL/6 FAP-/- mice. On the other hand, double positive T cells ($CD4^+CD8^+$) represented a minor cell population of $CD3^+$ lymphocytes.

However, there was wide variability between samples in leukocyte composition in the mouse GBM microenvironment (Fig. 20A, 21A).

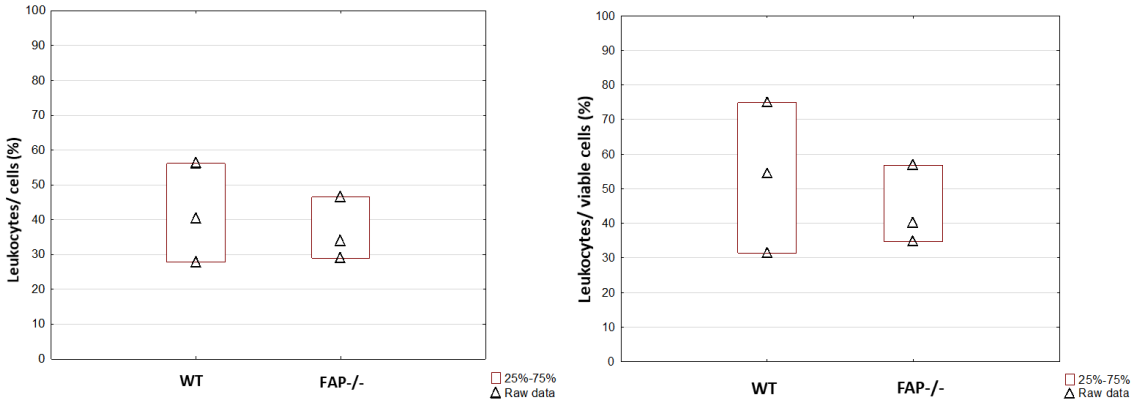

Figure 16: Percentage of leukocytes in the GBM microenvironment of C57BL/6J WT and C57BL/6 FAP-/- mice

Flow cytometric analysis of leukocytes ($CD45^+$) in C57BL/6J WT and C57BL/6 FAP-/- mice – the percentage of leukocytes in the GBM microenvironment. Boxes: middle 25-75% of measured values; triangles: raw data; N=3 mice; ($CD45^+$ of all cells) p=1.0 (left); ($CD45^+$ of viable cells) p=1.0 (right); Mann Whitney U test

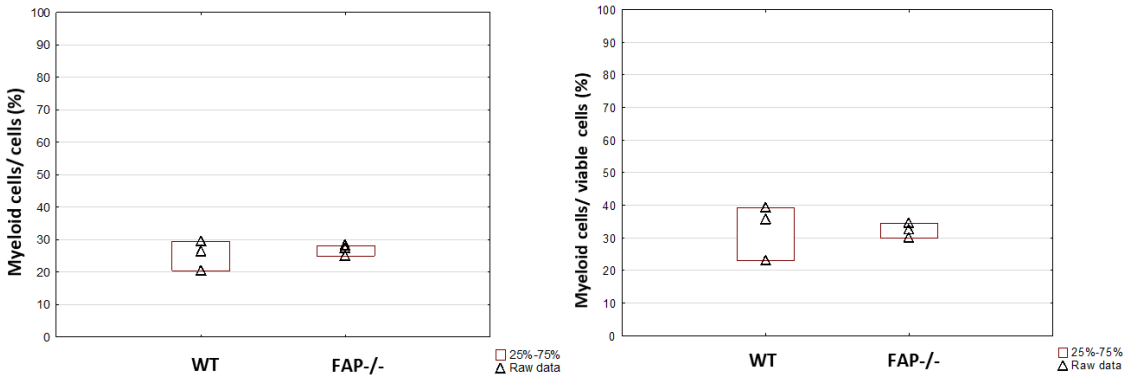

Figure 17: Percentage of myeloid cells in the GBM microenvironment of C57BL/6J WT and C57BL/6 FAP-/- mice:

Flow cytometric analysis of myeloid cells ($CD45^+F4/80^+$) in C57BL/6J WT and C57BL/6 FAP-/- mice – the percentage of myeloid cells in the GBM microenvironment. Boxes: middle 25-75% of measured values; triangles: raw data; N=3 mice; ($CD45^+F4/80^+$ of all cells) p=1.0 (left); ($CD45^+F4/80^+$ of viable cells) p=0.383 (right); Mann Whitney U test

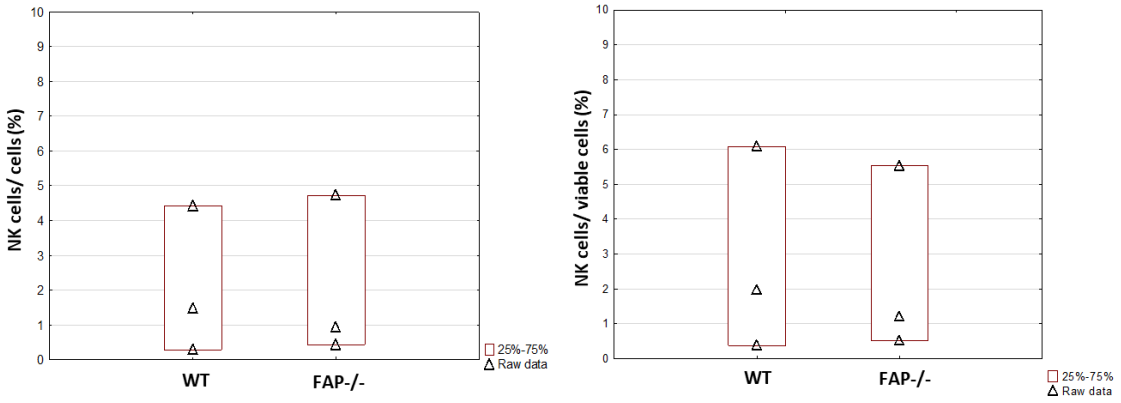

Figure 18: Percentage of NK cells in the GBM microenvironment of C57BL/6J WT and C57BL/6 FAP-/- mice

Flow cytometric analysis of NK cells ($CD45^+CD335^+CD3^-$) in C57BL/6J WT and C57BL/6 FAP-/- mice – the percentage of T cells in the GBM microenvironment. Boxes: middle 25-75% of measured values; triangles: raw data; N=3 mice; ($CD45^+CD335^+CD3^-$ of all cells) p=1.0 (left); ($CD45^+CD335^+CD3^-$ of viable cells) p=0.383 (right); Mann Whitney U test

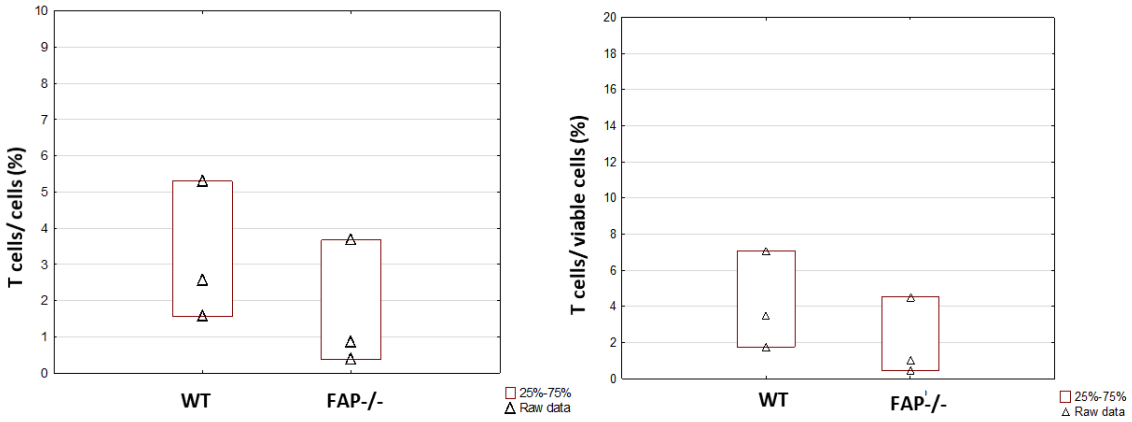

Figure 19: Percentage of T cells in the GBM microenvironment of C57BL/6J WT and C57BL/6 FAP-/- mice

Flow cytometric analysis of T cells ($CD45^+CD3^+$) in C57BL/6J WT and C57BL/6 FAP-/- mice – the percentage of T cells in the GBM microenvironment. Boxes: middle 25-75% of measured values; triangles: raw data; N=3 mice; ($CD45^+CD3^+$ of all cells) p=0.383 (left); ($CD45^+CD3^+$ of viable cells) p=0.383 (right); Mann Whitney U test

A)

	Myeloid cells (%)	T cells (%)	NK cells (%)
WT	65.3	6.39	3.38
	52.3	9.43	7.97
	73.6	5.62	1.19
FAP-/-	60.6	7.93	9.33
	86.2	1.31	1.62
	80.5	2.52	2.88

B)

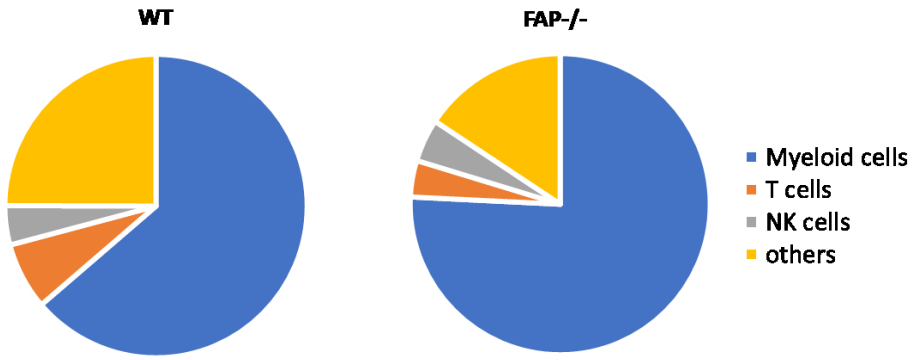

Figure 20: Composition of viable leukocytes in the GBM microenvironment of C57BL/6J WT and C57BL/6 FAP-/- mice

A) Raw data of viable leukocyte composition in the GBM microenvironment of C57BL/6J WT and C57BL/6 FAP-/- mice ***B)*** *Flow cytometric analysis of the viable leukocytes composition in the GBM microenvironment of C57BL/6J WT (left) and C57BL/6 FAP-/- (right) mice – the mean values of the percentages of immune subpopulations in the GBM microenvironment shown in pie charts; N=3; Myeloid cells (blue), T cells (orange), NK cells (grey) and others (yellow)*

A)

	$CD4^+$ T cells (%)	$CD4^+$ Treg/ $CD4^+$ T cells (%)	$CD8^+$ T cells (%)	DP T cells (%)	DN T cells (%)
WT	50.4	23.9	26.4	1.3	21.8
	51.9	27.8	25.4	2.4	20.3
	47.2	13.6	27.7	8.1	16.5
FAP-/-	38	20	31.3	4.4	32.9
	30,7	19.4	33.1	6.7	25.3
	44,4	11.9	23.5	2.0	28.6

B)

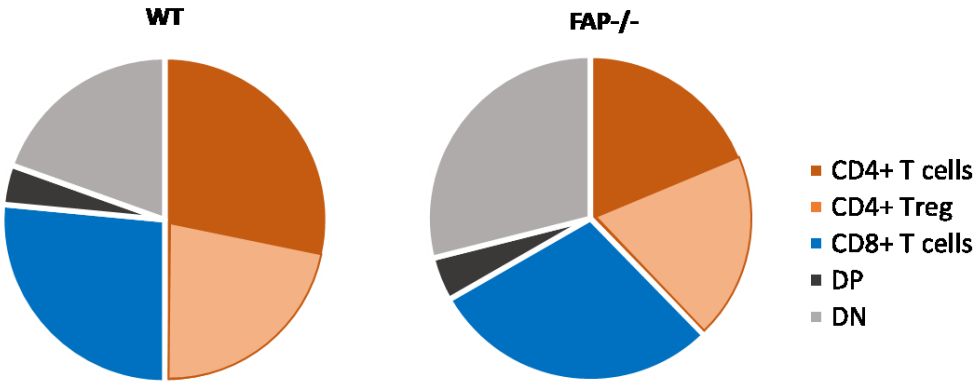

Figure 21: Composition of viable $CD3^+$ lymphocytes in the GBM microenvironment of C57BL/6J WT and C57BL/6 FAP-/- mice

A) *Raw data of viable $CD3^+$ lymphocytes composition in the GBM microenvironment of C57BL/6J WT and C57BL/6 FAP-/- mice* ***B)*** *Flow cytometric analysis of the viable $CD3^+$ lymphocyte composition in the GBM microenvironment of C57BL/6J WT (left) and C57BL/6 FAP-/- (right) mice – the mean values of the percentages of T cells in the GBM microenvironment shown in pie charts; N=3; all $CD4^+$ T cells (dark and light orange), $CD4^+$ Treg (light orange), $CD8^+$ T cells (blue), DP (black) and DN (grey)*

DP – $CD4^+CD8^+$ double positive T cells, DN – $CD4^-CD8^-$ double negative T cells

8. Discussion

Tumor microenvironment plays a pivotal role during tumor progression. GBM tumors are highly infiltrated with immune cells compared to the healthy non-tumorous brain. However, the GBM microenvironment is characterized by strong immunosuppression [175]. Immunosuppression in the tumor microenvironment is a consequence of dynamic interactions among the tumor, immune, and other stromal cells [28].

In various tumors, stromal cells expressing FAP were associated with specific infiltration of immune cells possessing immunosuppressive properties into the tumor microenvironment [58,87,90,91]. The role of these cell populations in the immune cell composition in the tumor microenvironment was also shown by the ablation of FAP^+ stromal cells [85,88,89].

We hypothesized that the expression of FAP modulates the immune cell composition in the tumor microenvironment of the mouse GBM model.

Flow cytometry is used as one of the methods to evaluate the tumor microenvironment composition due to its ability to detect different cell subpopulations.

To acquire reliable data by using flow cytometry, it is crucial to prepare a single cell suspension. The preparation of single cell suspension from solid tissue could be associated with the loss of cells of interest, reduced cell viability, or marker expression modification. All these parameters must be considered in the experimental design.

Literature evidence suggested that mechanical non-enzymatic dissociation of tissue led to the acquirement of cell suspensions with better cell viability in certain tumors (breast tumor) [152]. However, non-enzymatic digestion of tissue is associated with inconsistent cell yield due to an insufficient breakdown of cell-cell junctions and proteins of the extracellular matrix. Moreover, mechanical non-enzymatic dissociation tends to release the intracellular compartments and nucleic acids that lead to the formation of cell aggregates [148].

In various types of tissue, including brain tumors, enzymatically treated samples provided higher counts of viable cells in comparison to non-enzymatically treated samples [148,156,176,177]. However, enzymatic digestion of tissue could lead to the cleavage

of surface markers, or in contrast, cause higher detection of positive cell population due to better access to antibodies for the specific epitope [152,178].

The Brain Tumor Dissociation kit, specifically developed for brain tumors, was used for the isolation of myeloid cells from mouse GBM [166]. Nevertheless, the Tumor Dissociation kit is more suitable for the detection of lymphocytes in the tumor microenvironment, due to its minimal effects on the expressed surface markers of lymphocytes, according to the manufacturer.

In order to precisely detect immune subpopulations in the GBM microenvironment in our experimental design, optimization of the dissociation method was necessary. According to previous studies, four different methods were designed by using enzymatic and non-enzymatic digestion in tissue processing [152,165–167].

The methods were evaluated for viable cell yield and modification of surface immune markers. First, the designed protocols were evaluated on mouse spleen tissues to determine the loss of viable leukocytes during the tissue dissociation. The highest viability of leukocytes in cell suspension from the spleen was obtained by dissociation using the dissociator and Tumor Dissociation kit, whereas other dissociation methods caused significantly reduced leukocyte viability. Then, the protocols were applied to mouse GBM tissue to determine cell viability and viable leukocyte yield. Concordantly with the results in the spleen, the method using the dissociator and Tumor Dissociation kit led to satisfactory cell viability, and also this method provided the highest viable leukocyte yield.

To evaluate the possible effect of enzymatic treatment on the studied immune cell surface molecules in single cell suspensions, peritoneal macrophages, and blood lymphocytes were exposed to individual enzymes. Accutase and Tumor Dissociation kit had no significant effect on the surface expression of most tested molecules. Surprisingly, the cells treated by the Tumor Dissociation kit and accutase had a higher signal of CD335 molecule (a marker of natural killer cells) compared to the untreated control.

Based on these results, the method using dissociator and Tumor Dissociation kit was considered the most suitable for the dissociation of mouse GBM tissue for flow cytometry measurement.

The pilot experiment for the characterization of the composition of immune cells in the tumor microenvironment of GBM influenced by stromal FAP expression was conducted in the syngeneic glioblastoma model using wild-type and FAP knockout mice.

Immune subpopulations (myeloid cells, conventional T cells, regulatory T cells, and natural killer cells) were analyzed by surface and intracellular markers in cell suspension obtained from the mouse GBM tissue dissociated by the optimized method. Three panels were used to identify different immune subpopulations. Gating strategy for the identification of immune cells by flow cytometry included the exclusion of debris, doublets, and dead cells.

The results of the analysis showed that the pattern of infiltrated immune subpopulations into the tumor microenvironment was similar in both wild-type and FAP knockout mouse model of GBM. Similar to other studies, leukocytes represented a substantial portion of the GBM microenvironment [57,179–181].

The predominant immune subpopulation in both wild-type and FAP knockout syngeneic mouse models of GBM was comprised of myeloid cells. However, there was no difference in the frequencies of infiltrated myeloid cells in the GBM microenvironment in wild-type and FAP knockout mice. Interestingly, a similar pattern of infiltrated myeloid cells consisted of microglia and bone marrow-derived monocytes/macrophages, was also observed in human GBM [33,50,180,182].

In GBM tissue of both wild-type and FAP knockout mice, conventional T cells, regulatory T cells, and natural killer cells were detected, as described in other studies in mouse and human GBM [57,180]. $CD3^+CD4^+$ T cells tended to accumulate more in tumors of wild-type mice compared to FAP knockout mice. The fraction of $CD3^+CD8^+$ T cells was similar in both wild-type and FAP knockout mice. A minor lymphocyte fraction consisted of regulatory $CD4^+$ T cells in both wild-type mice FAP knockout mice. The infiltration of regulatory T cells in mouse tumor tissue was also observed in another study, where it was shown that the frequency of regulatory T cells does not significantly change in the brain during tumor progression [57]. Intratumoral $CD4^-CD8^-$ double negative T cells represented a considerable portion of $CD3^+$ lymphocytes in tumors of FAP knockout mice. The presence of these double negative cell population was observed to suppress tumor cell proliferation of human pancreatic cancer cells [183].

Nevertheless, there was no significant difference in the presence of these immune subpopulations between wild-type and FAP knockout mice.

FAP in the tumor microenvironment of various solid tumors is expressed mainly by cancer-associated fibroblasts (CAFs). It was shown that CAFs that express FAP are more potent to induce immunosuppression in the tumor microenvironment [58,94,95]. Stromal cell populations sharing similar phenotypic and functional properties with CAFs were identified in the GBM microenvironment [84,96].

FAP^+ stromal cells have been described to stimulate the infiltration of regulatory T cells and myeloid cells with immunosuppressive properties into the tumor microenvironment [58,91,94,184].

Moreover, higher FAP expression was correlated with a reduced presence of $CD3^+$ cells in the tumor microenvironment in colorectal cancer [94]. In accordance, one study has demonstrated that FAP knockout mice with pancreatic adenocarcinoma tended to have higher frequencies of $CD3^+$ lymphocytes at the tumor site [185].

Also, higher FAP activity was shown to significantly decreased the frequencies of $CD8^+$ T cells in tumors [58].

The mesenchymal subtype of GBM is linked to a more immunosuppressive microenvironment in comparison with other subtypes [98]. Also, the expression of FAP is associated with the mesenchymal subtype of GBM [84]. GL261 model shares similar characteristics with the mesenchymal subtype of GBM, and in one study, it is reported that infiltrated host mesenchymal cells correlate with tumor progression [181].

Detection of FAP enzymatic activity in our mouse model of GBM suggested that GL261 cell line has a rather low expression of FAP. However, FAP was detected in the healthy mouse brain and spleen besides other organs. In another study, FAP was also detected in other mouse organs of the immune system, like bone marrow and lymph nodes [186]. In humans, FAP expression was detected in bone marrow as well [79].

In human GBM, FAP is expressed mainly by mesenchymal-like cells and tumor cells [84]. In our GBM model, we tried to estimate if FAP expression on stromal cells could have an effect on immune cell composition in the GBM microenvironment and tumor progression. According to the acquired data, there was no significant difference in the

observed parameters of tumor progression like tumor volume or the frequencies of infiltrated immune subpopulations of interest between wild-type and FAP knockout mice.

This study has several potential limitations that are associated with the characterization of immune cell composition in the mouse GBM.

During the acquiring and analysis of cytometry data, there were some technical problems with cytometry setting and panel design. Surprisingly, in mouse brain tumor tissue, were atypical double-positive populations ($F4/80^+CD3^+$ and $CD3^+CD335^+$) detected. It was assumed that the detection of a double positive population might be a result of uncompensated data. A new compensation matrix was set on single stained samples of mouse whole blood and mouse peritoneal macrophages obtained by peritoneal lavage with the same antibodies and voltage settings as used in the analysis of mouse GBM tissues. Unfortunately, after applying a new compensation matrix, there were still double-positive populations. The reason for $CD3^+CD335^+$ cells might also be the instability of tandem dye. Antibody for CD335 marker was equipped with Phycoerythrin fluorophore, and an antibody for CD3 marker was conjugated with Phycoerythrin-Cyanine7. Antibodies conjugated with tandem Phycoerythrin-Cyanine7 are sensitive to light and get easily degraded. Therefore, a strong signal could be seen in the donor channel Phycoerythrin. However, even nondegradable tandem can provide some weaker signals in the donor channel.

Treg detection in cell suspension also had some technical issues. Longer incubation time during fixation and permeabilization of Treg in cell suspension caused cell aggregation, and single cell suspension lost its properties suitable for flow cytometry measurement. In this work, regulatory T cells were defined as $CD4^+CD25^+Helios^+$ cells. Another possible approach for Treg detection is the negativity of surface marker CD127. The marker CD127 is expressed by conventional T cells but not by Treg. Using only surface markers might be more suitable for further identification of Treg in the cell suspension obtained from dissociated tumor tissue [187].

Although slight trends indicate a difference in the composition of leukocytes between wild-type and FAP knockout mouse model of GBM, the results did not reach statistical significance. One of the possible reasons could be the use of small numbers of experimental groups.

In order to determine whether the composition of immune cells in the tumor microenvironment is influenced by stromal FAP expression, the experiment should have been conducted on larger groups of mice with a more detailed panel for flow cytometry measurement for further characterization of phenotypical properties of immune cells.

Nevertheless, this work provided an optimized protocol for preparing single cell suspensions from mouse GBM tissues suitable for flow cytometry analysis, which will be used in further studies of infiltrated immune subsets in mouse models of astrocytic tumors.

9. Conclusions

Protocol for mouse glioblastoma tissue dissociation and preparation of single cell suspension suitable for flow cytometry analysis was optimized.

The developed and optimized method:

- provides higher cell viability in cell suspension obtained from mouse GBM tissue compared to other dissociation methods
- provides high viable leukocyte yield
- minimizes alteration of studied marker expression in immune cells
- enables the detection of various immune subpopulations (myeloid cells, conventional T cells, regulatory T cells, and natural killer cells)

A pilot experiment of a flow cytometry analysis of immune cells in mouse GBM showed high infiltration of leukocytes, dominantly myeloid cells, into the tumor microenvironment. There were no statistically significant differences in the composition of intratumoral immune cells between wild-type and FAP knockout mice.

The optimized method will be applied to mouse models of astrocytic tumors for further characterization of phenotypic properties of immune cells in the tumor microenvironment.

10. References

1. Louis, D. N. *et al.* The 2016 World Health Organization Classification of Tumors of the Central Nervous System: a summary. *Acta Neuropathol.* **131**, 803–820 (2016).
2. Hu, N., Cheng, H., Zhang, K. & Jensen, R. Evaluating the Prognostic Accuracy of Biomarkers for Glioblastoma Multiforme Using The Cancer Genome Atlas Data. *Cancer Inform.* **16**, 117693511773484 (2017).
3. Ohgaki, H. & Kleihues, P. Epidemiology and etiology of gliomas. *Acta Neuropathol.* **109**, 93–108 (2005).
4. Ostrom, Q. T. *et al.* Sex-specific glioma genome-wide association study identifies new risk locus at 3p21.31 in females, and finds sex-differences in risk at 8q24.21. *Sci. Rep.* **8**, 1–15 (2018).
5. Thakkar, J. P. *et al.* Epidemiologic and molecular prognostic review of glioblastoma. *Cancer Epidemiology Biomarkers and Prevention* vol. 23 1985–1996 (2014).
6. Fisher et al., 2007. Epidemiology of Brain Tumors. *Neurol. Clin.* **25**, 867–890 (2007).
7. Kyritsis, A. P., Bondy, M. L., Rao, J. S. & Sioka, C. Inherited predisposition to glioma. *Neuro. Oncol.* **12**, 104–13 (2010).
8. Lee, J. H. *et al.* Human glioblastoma arises from subventricular zone cells with low-level driver mutations. *Nature* **560**, 243–247 (2018).
9. Ayob, A. Z. & Ramasamy, T. S. Cancer stem cells as key drivers of tumour progression. *J. Biomed. Sci.* **25**, 20 (2018).
10. Dirkse, A. *et al.* Stem cell-associated heterogeneity in Glioblastoma results from intrinsic tumor plasticity shaped by the microenvironment. *Nat. Commun.* **10**, 1–16 (2019).
11. Krell, D. *et al.* Screen for IDH1, IDH2, IDH3, D2HGDH and l2HGDH mutations in glioblastoma. *PLoS One* **6**, (2011).
12. Ohgaki, H. & Kleihues, P. The definition of primary and secondary glioblastoma. *Clinical Cancer Research* vol. 19 764–772 (2013).
13. Verhaak, R. G. W. *et al.* Integrated Genomic Analysis Identifies Clinically Relevant Subtypes of Glioblastoma Characterized by Abnormalities in PDGFRA, IDH1, EGFR, and NF1. *Cancer Cell* **17**, 98–110 (2010).
14. Wang, Q. *et al.* Tumor Evolution of Glioma-Intrinsic Gene Expression Subtypes Associates with Immunological Changes in the Microenvironment. *Cancer Cell* **32**, 42-56.e6 (2017).
15. Körber, V. *et al.* Evolutionary Trajectories of IDH WT Glioblastomas Reveal a Common Path of Early Tumorigenesis Instigated Years ahead of Initial Diagnosis. *Cancer Cell* **35**, 692-704.e12 (2019).
16. Wang, Q. *et al.* Tumor Evolution of Glioma Intrinsic Gene Expression Subtype Associates With Immunological Changes in the Microenvironment. *Neuro. Oncol.* **18**, vi202–vi202 (2016).
17. Quail et al., 2017. The Microenvironmental Landscape of Brain Tumors. *Cancer Cell* **31**, 326–341 (2017).
18. Hambardzumyan et al., 2015. Glioblastoma: Defining Tumor Niches. *Trends in Cancer*

1, 252–265 (2015).

19. Aspelund, A. *et al.* A dural lymphatic vascular system that drains brain interstitial fluid and macromolecules. *J. Exp. Med.* **212**, 991–9 (2015).

20. Louveau, A. *et al.* Structural and functional features of central nervous system lymphatic vessels. *Nature* **523**, 337–341 (2015).

21. Absinta, M. *et al.* Human and nonhuman primate meninges harbor lymphatic vessels that can be visualized noninvasively by MRI. *Elife* **6**, (2017).

22. Jani, R. H. & Sekula, R. F. Magnetic Resonance Imaging of Human Dural Meningeal Lymphatics. *Neurosurgery* (2018).

23. Louveau, A. *et al.* CNS lymphatic drainage and neuroinflammation are regulated by meningeal lymphatic vasculature. *Nat. Neurosci.* **21**, 1380–1391 (2018).

24. Noman, M. Z. *et al.* Blocking Hypoxia-Induced Autophagy in Tumors Restores Cytotoxic T-Cell Activity and Promotes Regression. *Cancer Res.* **71**, 5976–5986 (2011).

25. Noman, M. Z. *et al.* The Cooperative Induction of Hypoxia-Inducible Factor-1α and STAT3 during Hypoxia Induced an Impairment of Tumor Susceptibility to CTL-Mediated Cell Lysis. *J. Immunol.* **182**, 3510–3521 (2009).

26. Leten, C., Struys, T., Dresselaers, T. & Himmelreich, U. In vivo and ex vivo assessment of the blood brain barrier integrity in different glioblastoma animal models. *J. Neurooncol.* **119**, 297–306 (2014).

27. Hanahan, D. & Weinberg, R. A. Hallmarks of cancer: The next generation. *Cell* vol. 144 646–674 (2011).

28. Munhoz, R. R. & Postow, M. A. Recent advances in understanding antitumor immunity. *F1000Research* **5**, 2545 (2016).

29. Fecci, P. E. *et al.* Increased regulatory T-cell fraction amidst a diminished CD4 compartment explains cellular immune defects in patients with malignant glioma. *Cancer Res.* **66**, 3294–3302 (2006).

30. Chongsathidkiet, P. *et al.* Sequestration of T cells in bone marrow in the setting of glioblastoma and other intracranial tumors. *Nat. Med.* **24**, 1459–1468 (2018).

31. Gousias, K. *et al.* Frequent abnormalities of the immune system in gliomas and correlation with the WHO grading system of malignancy. *J. Neuroimmunol.* **226**, 136–142 (2010).

32. Woroniecka, K. *et al.* T-cell exhaustion signatures vary with tumor type and are severe in glioblastoma. *Clin. Cancer Res.* **24**, (2018).

33. Alban, T. J. *et al.* Global immune fingerprinting in glioblastoma patient peripheral blood reveals immune-suppression signatures associated with prognosis. *JCI insight* **3**, (2018).

34. Kmiecik, J. *et al.* Elevated CD3+ and CD8+ tumor-infiltrating immune cells correlate with prolonged survival in glioblastoma patients despite integrated immunosuppressive mechanisms in the tumor microenvironment and at the systemic level. *J. Neuroimmunol.* **264**, 71–83 (2013).

35. Pickup, M., Novitskiy, S. & Moses, H. L. The roles of TGFβ in the tumour microenvironment. *Nature Reviews Cancer* vol. 13 788–799 (2013).

36. Tamura, R. *et al.* The role of vascular endothelial growth factor in the hypoxic and immunosuppressive tumor microenvironment: perspectives for therapeutic implications.

Medical Oncology vol. 37 1–14 (2020).

37. Ueda, R. *et al.* Systemic inhibition of transforming growth factor-β in glioma-bearing mice improves the therapeutic efficacy of glioma-associated antigen peptide vaccines. *Clin. Cancer Res.* **15**, 6551–6559 (2009).

38. Turkowski, K. *et al.* VEGF as a modulator of the innate immune response in glioblastoma. *Glia* **66**, 161–174 (2018).

39. Soubéran, A. *et al.* Effects of VEGF blockade on the dynamics of the inflammatory landscape in glioblastoma-bearing mice. *J. Neuroinflammation* **16**, 191 (2019).

40. Alvarado, A. G. *et al.* Glioblastoma Cancer Stem Cells Evade Innate Immune Suppression of Self-Renewal through Reduced TLR4 Expression. *Cell Stem Cell* **20**, 450-461.e4 (2017).

41. Van Der Vos, K. E. *et al.* Directly visualized glioblastoma-derived extracellular vesicles transfer RNA to microglia/macrophages in the brain. *Neuro. Oncol.* **18**, 58–69 (2016).

42. Freeman, G. J. *et al.* Engagement of the PD-1 immunoinhibitory receptor by a novel B7 family member leads to negative regulation of lymphocyte activation. *J. Exp. Med.* **192**, 1027–1034 (2000).

43. Ricklefs, F. L. *et al.* Immune evasion mediated by PD-L1 on glioblastoma-derived extracellular vesicles. *Sci. Adv.* **4**, (2018).

44. Gratas, C. *et al.* Fas ligand expression in glioblastoma cell lines and primary astrocytic brain tumors. *Brain Pathol.* **7**, 863–9 (1997).

45. Badie, B., Schartner, J., Prabakaran, S., Paul, J. & Vorpahl, J. Expression of Fas ligand by microglia: Possible role in glioma immune evasion. *J. Neuroimmunol.* **120**, 19–24 (2001).

46. Henrik Heiland, D. *et al.* Tumor-associated reactive astrocytes aid the evolution of immunosuppressive environment in glioblastoma. *Nat. Commun.* **10**, (2019).

47. Norden et al., 2014. TGFβ produced by IL-10 redirected astrocytes attenuates microglial activation. *Glia* **62**, 881–895 (2014).

48. Ding, A. S., Routkevitch, D., Jackson, C. & Lim, M. Targeting Myeloid Cells in Combination Treatments for Glioma and Other Tumors. *Frontiers in immunology* vol. 10 1715 (2019).

49. Böttcher, C. *et al.* Human microglia regional heterogeneity and phenotypes determined by multiplexed single-cell mass cytometry. *Nat. Neurosci.* **22**, 78–90 (2019).

50. Chang, A. L. *et al.* CCL2 produced by the glioma microenvironment is essential for the recruitment of regulatory t cells and myeloid-derived suppressor cells. *Cancer Res.* **76**, 5671–5682 (2016).

51. Wang, S.-C., Hong, J.-H., Hsueh, C. & Chiang, C.-S. Tumor-secreted SDF-1 promotes glioma invasiveness and TAM tropism toward hypoxia in a murine astrocytoma model. *Lab. Investig.* **92**, 151–162 (2012).

52. Sielska, M. *et al.* Distinct roles of CSF family cytokines in macrophage infiltration and activation in glioma progression and injury response. *J. Pathol.* **230**, 310–321 (2013).

53. Yi, L. *et al.* Glioma-initiating cells: a predominant role in microglia/macrophages tropism to glioma. *J. Neuroimmunol.* **232**, 75–82 (2011).

54. Osterberg, N. *et al.* Decrease of VEGF-A in myeloid cells attenuates glioma progression

and prolongs survival in an experimental glioma model. *Neuro. Oncol.* **18**, 939–49 (2016).

55. Carvalho da Fonseca, A. C. *et al.* Increased expression of stress inducible protein 1 in glioma-associated microglia/macrophages. *J. Neuroimmunol.* **274**, 71–7 (2014).

56. Kamran, N. *et al.* Immunosuppressive Myeloid Cells' Blockade in the Glioma Microenvironment Enhances the Efficacy of Immune-Stimulatory Gene Therapy. *Mol. Ther.* **25**, 232–248 (2017).

57. Zhang, I. *et al.* Characterization of Arginase Expression in Glioma-Associated Microglia and Macrophages. *PLoS One* **11**, e0165118 (2016).

58. Yang, X. *et al.* FAP Promotes Immunosuppression by Cancer-Associated Fibroblasts in the Tumor Microenvironment via STAT3–CCL2 Signaling. *Cancer Res.* **76**, 4124–4135 (2016).

59. Han, S. *et al.* Tumour-infiltrating CD4+ and CD8+ lymphocytes as predictors of clinical outcome in glioma. *Br. J. Cancer* **110**, 2560–2568 (2014).

60. Patel, M. A. *et al.* Agonist anti-GITR monoclonal antibody and stereotactic radiation induce immune-mediated survival advantage in murine intracranial glioma. *J. Immunother. Cancer* **4**, 1–13 (2016).

61. Miska, J. *et al.* HIF-1α Is a Metabolic Switch between Glycolytic-Driven Migration and Oxidative Phosphorylation-Driven Immunosuppression of Tregs in Glioblastoma. *Cell Rep.* **27**, 226-237.e4 (2019).

62. Takahashi, T. *et al.* Imunologic self-tolerance maintained by CD25+CD4+ regulatory T cells constitutively expressing cytotoxic T lymphocyte-associated antigen 4. *J. Exp. Med.* **192**, 303–310 (2000).

63. Agarwalla, P., Barnard, Z., Fecci, P., Dranoff, G. & Curry, W. T. Sequential immunotherapy by vaccination with GM-CSF-expressing glioma cells and CTLA-4 blockade effectively treats established murine intracranial tumors. *J. Immunother.* **35**, 385–389 (2012).

64. Xiao, Z. X. *et al.* Identification of repaglinide as a therapeutic drug for glioblastoma multiforme. *Biochem. Biophys. Res. Commun.* **488**, 33–39 (2017).

65. Curtin, J. F. *et al.* Treg depletion inhibits efficacy of cancer immunotherapy: Implications for clinical trials. *PLoS One* **3**, (2008).

66. Balabanov et al., 1996. CNS microvascular pericytes express macrophage-like function, cell surface integrin αM, and macrophage marker ED-2. *Microvasc. Res.* **52**, 127–142 (1996).

67. Valdor, R. *et al.* Glioblastoma ablates pericytes antitumor immune function through aberrant up-regulation of chaperone-mediated autophagy. *Proc. Natl. Acad. Sci. U. S. A.* **116**, 20655–20665 (2019).

68. Valdor, R. *et al.* Glioblastoma progression is assisted by induction of immunosuppressive function of pericytes through interaction with tumor cells. *Oncotarget* **8**, 68614 (2017).

69. Ochs, K. *et al.* Immature mesenchymal stem cell-like pericytes as mediators of immunosuppression in human malignant glioma. *J. Neuroimmunol.* **265**, 106–116 (2013).

70. Tumangelova-Yuzeir, K. *et al.* Mesenchymal stem cells derived and cultured from glioblastoma multiforme increase tregs, downregulate th17, and induce the tolerogenic

phenotype of monocyte-derived cells. *Stem Cells Int.* **2019**, (2019).

71. Eatemadi, A. *et al.* Role of protease and protease inhibitors in cancer pathogenesis and treatment. *Biomedicine and Pharmacotherapy* vol. 86 221–231 (2017).

72. Goldstein, L. A. *et al.* Molecular cloning of seprase: A serine integral membrane protease from human melanoma. *Biochim. Biophys. Acta - Mol. Basis Dis.* (1997) doi:10.1016/S0925-4439(97)00032-X.

73. Aertgeerts, K. *et al.* Structural and kinetic analysis of the substrate specificity of human fibroblast activation protein alpha. *J. Biol. Chem.* **280**, 19441–4 (2005).

74. Niedermeyer, J. *et al.* Mouse fibroblast-activation protein - Conserved Fap gene organization and biochemical function as a serine protease. *Eur. J. Biochem.* **254**, 650–654 (1998).

75. Hamson, E. J., Keane, F. M., Tholen, S., Schilling, O. & Gorrell, M. D. Understanding fibroblast activation protein (FAP): Substrates, activities, expression and targeting for cancer therapy. *Proteomics - Clinical Applications* vol. 8 454–463 (2014).

76. Wong, P. F. *et al.* Neuropeptide y is a physiological substrate of fibroblast activation protein: Enzyme kinetics in blood plasma and expression of Y2R and Y5R in human liver cirrhosis and hepatocellular carcinoma. *Peptides* **75**, 80–95 (2016).

77. Dunshee, D. R. *et al.* Fibroblast activation protein cleaves and inactivates fibroblast growth factor 21. *J. Biol. Chem.* **291**, 5986–5996 (2016).

78. Busek et al. Co-expression of the homologous proteases fibroblast activation protein and dipeptidyl peptidase-IV in the adult human Langerhans islets. *Histochem. Cell Biol.* **143**, 497–504 (2015).

79. Bae, S. *et al.* Fibroblast activation protein α identifies mesenchymal stromal cells from human bone marrow. *Br. J. Haematol.* **142**, 827–830 (2008).

80. Dolznig, H. *et al.* Characterization of cancer stroma markers: in silico analysis of an mRNA expression database for fibroblast activation protein and endosialin. *Cancer Immun.* **5**, 10 (2005).

81. Tan, S. Y., Chowdhury, S., Polak, N., Gorrell, M. D. & Weninger, W. Fibroblast activation protein is dispensable in the anti-influenza immune response in mice. *PLoS One* **12**, (2017).

82. Roberts, E. W. *et al.* Depletion of stromal cells expressing fibroblast activation protein-α from skeletal muscle and bone marrow results in cachexia and anemia. *J. Exp. Med.* **210**, 1137–1151 (2013).

83. Huang, Y. *et al.* Isolation of Fibroblast-Activation Protein-Specific Cancer-Associated Fibroblasts. *Biomed Res. Int.* **2017**, 1–8 (2017).

84. Busek, P. *et al.* Fibroblast activation protein alpha is expressed by transformed and stromal cells and is associated with mesenchymal features in glioblastoma. *Tumor Biol.* **37**, 13961–13971 (2016).

85. Kraman, M. *et al.* Suppression of antitumor immunity by stromal cells expressing fibroblast activation protein-α. *Science (80-.).* **330**, 827–830 (2010).

86. Arnold, J. N., Magiera, L., Kraman, M. & Fearon, D. T. Tumoral immune suppression by macrophages expressing fibroblast activation protein-α and heme oxygenase-1. *Cancer Immunol. Res.* **2**, 121–126 (2014).

87. Hou, C. M. *et al.* Fibroblast activation proteins-α suppress tumor immunity by regulating

T cells and tumor-associated macrophages. *Exp. Mol. Pathol.* **104**, 29–37 (2018).

88. Wen, X. *et al.* Fibroblast activation protein-α-positive fibroblasts promote gastric cancer progression and resistance to immune checkpoint blockade. *Oncol. Res.* **25**, 629–640 (2017).

89. Zhang, Y. & Ertl, H. C. J. Depletion of FAP+ cells reduces immunosuppressive cells and improves metabolism and functions CD8+T cells within tumors. *Oncotarget* **7**, 23282–23299 (2016).

90. Higashino, N. *et al.* Fibroblast activation protein-positive fibroblasts promote tumor progression through secretion of CCL2 and interleukin-6 in esophageal squamous cell carcinoma. *Lab. Investig.* **99**, 777–792 (2019).

91. Takahashi, H. *et al.* Cancer-associated fibroblasts promote an immunosuppressive microenvironment through the induction and accumulation of protumoral macrophages. *Oncotarget* **8**, 8633–8647 (2017).

92. Cremasco, V. *et al.* FAP delineates heterogeneous and functionally divergent stromal cells in immune-excluded breast tumors. *Cancer Immunol. Res.* **6**, 1472–1485 (2018).

93. Lukacs-Kornek, V. *et al.* Regulated release of nitric oxide by nonhematopoietic stroma controls expansion of the activated T cell pool in lymph nodes. *Nat. Immunol.* **12**, 1096–1104 (2011).

94. Chen, L., Qiu, X., Wang, X. & He, J. FAP positive fibroblasts induce immune checkpoint blockade resistance in colorectal cancer via promoting immunosuppression. *Biochem. Biophys. Res. Commun.* **487**, 8–14 (2017).

95. Son, G. M. *et al.* Comparisons of cancer-associated fibroblasts in the intratumoral stroma and invasive front in colorectal cancer. *Med. (United States)* **98**, (2019).

96. Clavreul, A. *et al.* Glioblastoma-associated stromal cells (GASCs) from histologically normal surgical margins have a myofibroblast phenotype and angiogenic properties. *J. Pathol.* **233**, 74–88 (2014).

97. R. Mentlein et al., 2011. Expression and role of the cell surface protease seprase/fibroblast activation protein-α (FAP-α) in astroglial tumors. *Biol. Chem.* **392**, 199–207 (2011).

98. Park, J. *et al.* Transcriptome profiling-based identification of prognostic subtypes and multi-omics signatures of glioblastoma. *Sci. Rep.* **9**, (2019).

99. Kaffes, I. *et al.* Human Mesenchymal glioblastomas are characterized by an increased immune cell presence compared to Proneural and Classical tumors. *Oncoimmunology* **8**, (2019).

100. Martinez-Lage, M. *et al.* Immune landscapes associated with different glioblastoma molecular subtypes. *Acta Neuropathol. Commun.* **7**, 203 (2019).

101. Miyai, M. *et al.* Current trends in mouse models of glioblastoma. *J. Neurooncol.* **135**, 423–432 (2017).

102. Ausman, J. I., Shapiro, W. R. & Rall, D. P. Studies on the chemotherapy of experimental brain tumors: development of an experimental model. *Cancer Res.* **30**, 2394–400 (1970).

103. Yi, L. *et al.* Implantation of GL261 neurospheres into C57/BL6 mice: A more reliable syngeneic graft model for research on glioma-initiating cells. *Int. J. Oncol.* **43**, 477–484 (2013).

104. Szatmári, T. *et al.* Detailed characterization of the mouse glioma 261 tumor model for

experimental glioblastoma therapy. *Cancer Sci.* **97**, 546–553 (2006).

105. Zagzag, D. *et al.* Vascular apoptosis and involution in gliomas precede neovascularization: A novel concept for glioma growth and angiogenesis. *Lab. Investig.* **80**, 837–849 (2000).

106. Villamañan, L. *et al.* Up-Regulation of the Alpha Prime Subunit of Protein Kinase CK2 as a Marker of Fast Proliferation in GL261 Cultured Cells. *Pathol. Oncol. Res.* **25**, 1659–1663 (2019).

107. Genoud, V. *et al.* Responsiveness to anti-PD-1 and anti-CTLA-4 immune checkpoint blockade in SB28 and GL261 mouse glioma models. *Oncoimmunology* **7**, (2018).

108. Demaria, S. *et al.* The Combination of Ionizing Radiation and Peripheral Vaccination Produces Long-Term Survival of Mice Bearing Invasive GL261 Glioma. *Int. J. Radiat. Oncol.* **63**, S171 (2005).

109. Newcomb, E. W. *et al.* Flavopiridol inhibits the growth of GL261 gliomas in vivo: implications for malignant glioma therapy. *Cell Cycle* **3**, 230–234 (2004).

110. Ginhoux, F. *et al.* Fate mapping analysis reveals that adult microglia derive from primitive macrophages. *Science* **330**, 841–5 (2010).

111. Prinz, M. & Priller, J. The role of peripheral immune cells in the CNS in steady state and disease. *Nat. Neurosci.* **20**, 136–144 (2017).

112. Lawson, L. J., Perry, V. H. & Gordon, S. Turnover of resident microglia in the normal adult mouse brain. *Neuroscience* **48**, 405–415 (1992).

113. Hickey, W. F. & Kimura, H. Perivascular microglial cells of the CNS are bone marrow-derived and present antigen in vivo. *Science* **239**, 290–2 (1988).

114. Gehrmann, J., Matsumoto, Y. & Kreutzberg, G. W. Microglia: intrinsic immuneffector cell of the brain. *Brain Res. Brain Res. Rev.* **20**, 269–87 (1995).

115. Badie, B. & Schartner, J. M. Flow Cytometric Characterization of Tumor-associated Macrophages in Experimental Gliomas. *Neurosurgery* **46**, 957–962 (2000).

116. Bennett, M. L. *et al.* New tools for studying microglia in the mouse and human CNS. *Proc. Natl. Acad. Sci. U. S. A.* **113**, E1738-46 (2016).

117. Bertolini, T. B. *et al.* Genetic background affects the expansion of macrophage subsets in the lungs of Mycobacterium tuberculosis-infected hosts. *Immunology* **148**, 102–113 (2016).

118. Zhu, Y. *et al.* Identification of different macrophage subpopulations with distinct activities in a mouse model of oxygen-induced retinopathy. *Int. J. Mol. Med.* **40**, 281–292 (2017).

119. Ajami, B. *et al.* Single-cell mass cytometry reveals distinct populations of brain myeloid cells in mouse neuroinflammation and neurodegeneration models. *Nat. Neurosci.* **21**, 541–551 (2018).

120. Fountain, E., Esparza, T., Malkova, O., Oh, S. & Brody, D. Microglial Heterogeneity in a Mouse Model of Alzheimer's Disease: A Mass Cytometry Analysis. *bioRxiv* 404178 (2018) doi:10.1101/404178.

121. Zemmour, D. *et al.* Single-cell gene expression reveals a landscape of regulatory T cell phenotypes shaped by the TCR article. *Nat. Immunol.* **19**, 291–301 (2018).

122. Ephrem, A. *et al.* Modulation of Treg cells/T effector function by GITR signaling is

context-dependent. *Eur. J. Immunol.* **43**, 2421–2429 (2013).

123. Thornton, A. M. *et al.* Expression of Helios, an Ikaros Transcription Factor Family Member, Differentiates Thymic-Derived from Peripherally Induced Foxp3 + T Regulatory Cells . *J. Immunol.* **184**, 3433–3441 (2010).

124. Graham, J. B. *et al.* Extensive Homeostatic T Cell Phenotypic Variation within the Collaborative Cross. *Cell Rep.* **21**, 2313–2325 (2017).

125. Lee, J. Y. *et al.* Phenotypic and functional changes of peripheral Ly6C+ T regulatory cells driven by conventional effector T cells. *Front. Immunol.* **9**, (2018).

126. Toomer, K. H. *et al.* Developmental Progression and Interrelationship of Central and Effector Regulatory T Cell Subsets. *J. Immunol.* **196**, 3665–3676 (2016).

127. Crinier, A. *et al.* High-Dimensional Single-Cell Analysis Identifies Organ-Specific Signatures and Conserved NK Cell Subsets in Humans and Mice. *Immunity* **49**, 971-986.e5 (2018).

128. Paul, S., Kulkarni, N., Shilpi, N. & Lal, G. Intratumoral natural killer cells show reduced effector and cytolytic properties and control the differentiation of effector Th1 cells. *Oncoimmunology* **5**, e1235106 (2016).

129. Walzer, T. *et al.* Identification, activation, and selective in vivo ablation of mouse NK cells via NKp46. *Proc. Natl. Acad. Sci. U. S. A.* **104**, 3384–9 (2007).

130. Hambardzumyan, D., Gutmann, D. H. & Kettenmann, H. The role of microglia and macrophages in glioma maintenance and progression. *Nat. Neurosci.* **19**, 20–7 (2016).

131. Bettelli, E. *et al.* Reciprocal developmental pathways for the generation of pathogenic effector TH17 and regulatory T cells. *Nature* **441**, 235–238 (2006).

132. Adeegbe, D. O. & Nishikawa, H. Natural and induced T regulatory cells in cancer. *Front. Immunol.* **4**, 190 (2013).

133. Wainwright, D. A., Sengupta, S., Han, Y. & Lesniak, M. S. Thymus-derived rather than tumor-induced regulatory T cells predominate in brain tumors. *Neuro. Oncol.* **13**, 1308–23 (2011).

134. Ito, M. *et al.* Brain regulatory T cells suppress astrogliosis and potentiate neurological recovery. *Nature* **565**, 246–250 (2019).

135. Baecher-Allan, C., Brown, J. A., Freeman, G. J. & Hafler, D. A. CD4+CD25high regulatory cells in human peripheral blood. *J. Immunol.* **167**, 1245–53 (2001).

136. Fontenot, J. D., Rasmussen, J. P., Gavin, M. A. & Rudensky, A. Y. A function for interleukin 2 in Foxp3-expressing regulatory T cells. *Nat. Immunol.* **6**, 1142–1151 (2005).

137. Pandiyan, P., Zheng, L., Ishihara, S., Reed, J. & Lenardo, M. J. CD4+CD25+Foxp3+ regulatory T cells induce cytokine deprivation–mediated apoptosis of effector CD4+ T cells. *Nat. Immunol.* **8**, 1353–1362 (2007).

138. Chang, X. *et al.* The Scurfy mutation of FoxP3 in the thymus stroma leads to defective thymopoiesis. *J. Exp. Med.* **202**, 1141–51 (2005).

139. Wan, Y. Y. & Flavell, R. A. Regulatory T-cell functions are subverted and converted owing to attenuated Foxp3 expression. *Nature* **445**, 766–770 (2007).

140. Zhang, Z. *et al.* Activation and Functional Specialization of Regulatory T Cells Lead to the Generation of Foxp3 Instability. *J. Immunol.* **198**, 2612–2625 (2017).

141. Sebastian, M. *et al.* Helios Controls a Limited Subset of Regulatory T Cell Functions. *J. Immunol.* **196**, 144–155 (2016).

142. Kim, H. J. *et al.* Stable inhibitory activity of regulatory T cells requires the transcription factor Helios. *Science (80-.).* **350**, 334–339 (2015).

143. Mahmud, S. A. *et al.* Costimulation via the tumor-necrosis factor receptor superfamily couples TCR signal strength to the thymic differentiation of regulatory T cells. *Nat. Immunol.* **15**, 473–481 (2014).

144. Shimizu, J., Yamazaki, S., Takahashi, T., Ishida, Y. & Sakaguchi, S. Stimulation of CD25+CD4+ regulatory T cells through GITR breaks immunological self-tolerance. *Nat. Immunol.* **3**, 135–142 (2002).

145. Vivier, E. *et al.* Innate or adaptive immunity? The example of natural killer cells. *Science* **331**, 44–9 (2011).

146. Korin, B. *et al.* High-dimensional, single-cell characterization of the brain's immune compartment. *Nat. Neurosci.* **20**, 1300–1309 (2017).

147. He, H. *et al.* NK cells promote neutrophil recruitment in the brain during sepsis-induced neuroinflammation. *Sci. Rep.* **6**, 1–14 (2016).

148. Jager, L. D. *et al.* Effect of enzymatic and mechanical methods of dissociation on neural progenitor cells derived from induced pluripotent stem cells. **61**, 78–84 (2017).

149. Neeley, S. P. & Conley, F. K. Extraction and immunocytochemical characterization of viable mononuclear inflammatory cells from brains of mice with chronic Toxoplasma gondii infection. *J. Neuroimmunol.* (1987) doi:10.1016/0165-5728(87)90090-7.

150. Dick, A. D., Pell, M., Brew, B. J., Foulcher, E. & Sedgwick, J. D. Direct ex vivo flow cytometric analysis of human microglial cell CD4 expression: Examination of central nervous system biopsy specimens from HIV-seropositive patients and patients with other neurological disease. *AIDS* (1997) doi:10.1097/00002030-199714000-00006.

151. Barnas et al. Reciprocal Functional Modulation of the Activation of T Lymphocytes and Fibroblasts Derived from Human Solid Tumors. *J. Immunol.* **185**, 2681–2692 (2010).

152. Migliori, E. *et al.* A Simple and Rapid Protocol to Non-enzymatically Dissociate Fresh Human Tissues for the Analysis of Infiltrating Lymphocytes. *J. Vis. Exp.* (2014) doi:10.3791/52392.

153. Rustenhoven, J. *et al.* Isolation of highly enriched primary human microglia for functional studies. *Sci. Rep.* **6**, (2016).

154. Zhang, Y. *et al.* Purification and Characterization of Progenitor and Mature Human Astrocytes Reveals Transcriptional and Functional Differences with Mouse. *Neuron* **89**, 37–53 (2016).

155. Oliver, T. G. *et al.* Loss of patched and disruption of granule cell development in a pre-neoplastic stage of medulloblastoma. *Development* **132**, 2425–2439 (2005).

156. Volovitz, I. *et al.* A non-aggressive, highly efficient, enzymatic method for dissociation of human brain-tumors and brain-tissues to viable single-cells. *BMC Neurosci.* **17**, 1–10 (2016).

157. Pistollato, F. *et al.* Optimized Flow Cytometric Analysis of Central Nervous System Tissue Reveals Novel Functional Relationships Among Cells Expressing CD133, CD15, and CD24. *Stem Cells* (2007) doi:10.1634/stemcells.2006-0260.

158. Stremnitzer, C. *et al.* Papain degrades tight junction proteins of human keratinocytes in

vitro and sensitizes C57BL/6 mice via the skin independent of its enzymatic activity or TLR4 activation. *J. Invest. Dermatol.* (2015) doi:10.1038/jid.2015.58.

159. Price, P. A. The essential role of Ca2+in the activity of bovine pancreatic deoxyribonuclease. *J. Biol. Chem.* (1975).

160. Wolburg, H. *et al.* Modulation of tight junction structure in blood-brain barrier endothelial cells. Effects of tissue culture, second messengers and cocultured astrocytes. *J. Cell Sci.* **107 (Pt 5)**, 1347–57 (1994).

161. Machi, T., Kassell, N. F. & Scheld, W. M. Isolation and characterization of endothelial cells from bovine cerebral arteries. *In Vitro Cell. Dev. Biol.* **26**, 291–300 (1990).

162. Hussein, D. *et al.* Pediatric brain tumor cancer stem cells: cell cycle dynamics, DNA repair, and etoposide extrusion. *Neuro. Oncol.* **13**, 70–83 (2011).

163. Veshchev, I. *et al.* A non-aggressive, highly efficient, enzymatic method for dissociation of human brain-tumors and brain-tissues to viable single-cells. *BMC Neurosci.* **17**, 1–10 (2016).

164. Bajpai, R., Lesperance, J., Kim, M. & Terskikh, A. V. Efficient propagation of single cells accutase-dissociated human embryonic stem cells. *Mol. Reprod. Dev.* (2008) doi:10.1002/mrd.20809.

165. Robinson, A. P., Rodgers, J. M., Goings, G. E. & Miller, S. D. Characterization of oligodendroglial populations in mouse demyelinating disease using flow cytometry: Clues for MS pathogenesis. *PLoS One* (2014) doi:10.1371/journal.pone.0107649.

166. Bowman, R. L. *et al.* Macrophage Ontogeny Underlies Differences in Tumor-Specific Education in Brain Malignancies. *Cell Rep.* **17**, 2445–2459 (2016).

167. Pinton, L. *et al.* The immune suppressive microenvironment of human gliomas depends on the accumulation of bone marrow-derived macrophages in the center of the lesion. *J. Immunother. Cancer* **7**, 58 (2019).

168. Trylcova, J. *et al.* Effect of cancer-associated fibroblasts on the migration of glioma cells in vitro. *Tumor Biol.* **36**, 5873–5879 (2015).

169. Baumann, B. C., Dorsey, J. F., Benci, J. L., Joh, D. Y. & Kao, G. D. Stereotactic intracranial implantation and in vivo bioluminescent imaging of tumor xenografts in a mouse model system of glioblastoma multiforme. *J. Vis. Exp.* (2012) doi:10.3791/4089.

170. Baker, G. J., Castro, M. G. & Lowenstein, P. R. Isolation and Flow Cytometric Analysis of Glioma-infiltrating Peripheral Blood Mononuclear Cells. *J. Vis. Exp.* (2015) doi:10.3791/53676.

171. Mayhew, T. M. & Olsen, D. R. Magnetic resonance imaging (MRI) and model-free estimates of brain volume determined using the Cavalieri principle. *J. Anat.* **178**, 133–44 (1991).

172. Zhu, T. *et al.* Functional role of FcγRIIB in the regulation of mesenchymal stem cell function. *Int. J. Med. Sci.* **13**, 154–160 (2016).

173. Unkeless, J. C. Heterogeneity of human and murine Fc gamma receptors. *Ciba Found. Symp.* **118**, 89–101 (1986).

174. Park, J. E. *et al.* Fibroblast activation protein, a dual specificity serine protease expressed in reactive human tumor stromal fibroblasts. *J. Biol. Chem.* **274**, 36505–36512 (1999).

175. Antunes, A. R. P. *et al.* Understanding the glioblastoma immune microenvironment as basis for the development of new immunotherapeutic strategies. *Elife* **9**, (2020).

176. Zver, T., Mouloungui, E., Berdin, A., Roux, C. & Amiot, C. Validation of an automated technique for ovarian cortex dissociation: Isolation of viable ovarian cells and their qualification by multicolor flow cytometry. *J. Ovarian Res.* **10**, (2017).

177. Leelatian, N. *et al.* Single cell analysis of human tissues and solid tumors with mass cytometry. *Cytom. Part B - Clin. Cytom.* **92**, 68–78 (2017).

178. Autengruber, A., Gereke, M., Hansen, G., Hennig, C. & Bruder, D. Impact of enzymatic tissue disintegration on the level of surface molecule expression and immune cell function. *Eur. J. Microbiol. Immunol. (Bp).* **2**, 112–20 (2012).

179. Masson, F. *et al.* Brain Microenvironment Promotes the Final Functional Maturation of Tumor-Specific Effector CD8 + T Cells. (2007) doi:10.4049/jimmunol.179.2.845.

180. Klemm, F. *et al.* Resource Interrogation of the Microenvironmental Landscape in Brain Tumors Reveals Disease-Specific Alterations of Immune Cells ll Resource Interrogation of the Microenvironmental Landscape in Brain Tumors Reveals Disease-Specific Alterations of Immune Ce. *Cell* **181**, 1643-1660.e17 (2020).

181. Behnan, J. *et al.* Recruited brain tumor-derived mesenchymal stem cells contribute to brain tumor progression. *Stem Cells* **32**, 1110–1123 (2014).

182. Hutter, G. *et al.* Microglia are effector cells of CD47-SIRPα antiphagocytic axis disruption against glioblastoma. *Proc. Natl. Acad. Sci. U. S. A.* **116**, (2019).

183. Lu, Y. *et al.* Double-negative T Cells Inhibit Proliferation and Invasion of Human Pancreatic Cancer Cells in Co-culture. *Anticancer Res.* **39**, 5911–5918 (2019).

184. Zhou, J. *et al.* Cancer-Associated Fibroblasts Correlate with Tumor-Associated Macrophages Infiltration and Lymphatic Metastasis in Triple Negative Breast Cancer Patients. *J. Cancer* **9**, 4635 (2018).

185. Gunderson, A. J. *et al.* Blockade of fibroblast activation protein in combination with radiation treatment in murine models of pancreatic adenocarcinoma. *PLoS One* **14**, (2019).

186. Keane, F. M. *et al.* Quantitation of fibroblast activation protein (FAP)-specific protease activity in mouse, baboon and human fluids and organs. *FEBS Open Bio* **4**, 43–54 (2014).

187. Rodríguez-Perea, A. L., Arcia, E. D., Rueda, C. M. & Velilla, P. A. Phenotypical characterization of regulatory T cells in humans and rodents. *Clin. Exp. Immunol.* **185**, 281–91 (2016).